



Enhancing the alignment of the optically bright *Gaia* reference frame with respect to the International Celestial Reference System

Susanne Lunz^{1,2} , James M. Anderson^{2,1}, Ming H. Xu^{3,4,1} , Oleg Titov⁵, Robert Heinkelmann¹, Megan C. Johnson⁶, and Harald Schuh^{2,1}

¹ GFZ German Research Centre for Geosciences, 14473 Potsdam, Telegrafenberg, Germany
e-mail: susanne.lunz@gfz-potsdam.de

² Technische Universität Berlin, Chair of Satellite Geodesy, Kaiserin-Augusta-Allee 104-106, 10553 Berlin, Germany

³ Aalto University Metsähovi Radio Observatory, Metsähovintie 114, 02540 Kylmälä, Finland

⁴ Aalto University Department of Electronics and Nanoengineering, PL15500, 00076 Aalto, Finland

⁵ Geoscience Australia, PO Box 378, Canberra 2601, Australia

⁶ United States Naval Observatory (USNO), 3450 Massachusetts Ave NW, Washington, DC 20392, USA

Received 31 December 2020 / Accepted 10 May 2023

ABSTRACT

Context. The link of the *Gaia* frame in terms of non-rotation with respect to the International Celestial Reference System (ICRS), which is realized via very long baseline interferometry (VLBI) at radio wavelengths, has to be conducted for the wide range of optical magnitudes in which the spacecraft observes. There is a sufficient number of suitable counterparts between the two measurement systems for optically faint objects. However, the number of common optically bright ($G \leq 13$ mag) objects is sparse as most are faint at radio frequencies, and only a few objects suitable for astrometry have been observed by VLBI in the past. As a result, rotation parameters for the optically bright *Gaia* reference frame are not yet determined with sufficient accuracy.

Aims. The verification of the *Gaia* bright frame of DR2 and EDR3 is enhanced by the reevaluation of existing VLBI observations and the addition of newly acquired data for a sample of optically bright radio stars.

Methods. Historical data from the literature were reevaluated, ensuring that the calibrator positions and uncertainties (used for the determination of the absolute star positions in the phase-referencing analysis) were updated and homogeneously referred to the ICRF3, the third realization of the International Celestial Reference Frame. We selected 46 suitable optically bright radio stars from the literature for new radio observations, out of which 32 were detected with the VLBA in continuum mode in the X or C band, along with radio-bright calibrators in the ICRF3. Improved *Gaia*-VLBI rotation parameters were obtained by adding new observations and utilizing more realistic estimates of the absolute position uncertainties for all phase-referenced radio observations.

Results. The homogenization greatly improved the steadiness of the results when the most discrepant stars were rejected one after another through a dedicated iterative process. For *Gaia* DR2, this homogenization reduced the magnitude of the orientation parameters to less than 0.5 mas but increased that of the spin parameters, with the largest component being the rotation around the Y axis. An adjustment of the position uncertainties improved the reliability of the orientation parameters and the goodness of fit for the iterative solutions. Introducing the new single-epoch positions to the analysis reduced the correlations between the rotation parameters. The final spin for *Gaia* DR2 as determined by VLBI observations of radio stars is $(-0.056, -0.113, +0.033) \pm (0.046, 0.058, 0.053)$ mas yr⁻¹. A comparison of the new results with external, independently derived spin parameters for *Gaia* DR2 reveals smaller differences than when using the historical data from the literature. Applying the VLBI data to *Gaia* EDR3, which was already corrected for spin during *Gaia* processing, the derived residual spin is $(+0.022, +0.065, -0.016) \pm (0.024, 0.026, 0.024)$ mas yr⁻¹, showing that the component in Y is significant at the 2.4σ level.

Conclusions. Even though our analysis provides a more accurate frame tie, more VLBI data are needed to refine the results and reduce the scatter between iterative solutions.

Key words. astrometry – reference systems – radio continuum: stars – methods: data analysis – methods: observational – instrumentation: interferometers

1. Introduction

The *Gaia* spacecraft ([Gaia Collaboration 2016b](#)), operated by the European Space Agency (ESA) and launched in late 2013, has produced the most complete astrometric catalog of our Galaxy and the Local Group at optical wavelengths. In the first 22 months of its operations, it collected information about 1.7 billion objects, which was published as Data Release 2 (DR2; [Gaia Collaboration 2018](#)). Recently, the *Gaia* Early Data Release 3 (EDR3) was published, which is based on 34 months

of observations and contains new astrometric data for about 1.8 billion sources ([Gaia Collaboration 2021a](#)). These data already outperform any other astronomical catalog and will very likely remain the most accurate source of optical positions for several decades into the future. Thus, verifying *Gaia*'s orientation and spin, particularly for the time after mission end when spin and proper motion errors dominate the position errors, is essential for high-precision navigation and orientation in space. This especially holds for optically bright objects, which are regularly used for attitude control and are being tested for use in deep space

navigation beyond the medium Earth orbit (Martin-Mur et al. 2017, Optical Navigation Experiment¹).

A suitable measurement technique for linking the *Gaia* catalog to the International Celestial Reference System (ICRS; Arias et al. 1995) is geodetic very long baseline interferometry (VLBI). This measurement technique is regularly utilized by observing extragalactic compact radio sources and creating a celestial reference frame by solving for global positions of the radio sources from observations spanning more than 40 yr. The resulting catalogs reach a similar accuracy as that of *Gaia* DR2. The latest official realization is the Third International Celestial Reference Frame (ICRF3; Charlot et al. 2020), which was derived from data at S/X frequencies between March 1979 and March 2018. It includes positions for 4 536 objects with a noise floor of 30 microarcseconds (μas). For the first time, two further catalogs were published together with the S/X catalog, which list VLBI positions of radio sources from observations at 22 GHz and 32 GHz. These catalogs were aligned to the S/X catalog. The three catalogs also consider the effect of the galactocentric acceleration of the Solar System, which shows up in the data as effects with a global dipole pattern of apparent proper motions toward the Galactic center with an amplitude of $5.8 \mu\text{as yr}^{-1}$ (MacMillan et al. 2019). The positions consequently have an epoch, namely 2015.0. An unpublished prototype of this catalog was used to orient the *Gaia* DR2 catalog to the ICRS (2017-06-30, solution from GSFC, IAU Working Group Third Realization of International Celestial Reference Frame), and the spin was aligned to the prototype ICRF and AllWISE (mid-infrared) active galactic nucleus catalogs (Secrest et al. 2015, 2016). The alignment is confirmed to within $\pm 20 \mu\text{as}$ for orientation and $\pm 20 \mu\text{as yr}^{-1}$ for spin per axis (Lindgren et al. 2018) for the optically faint part of DR2, with a magnitude range of $G \gtrsim 15$ and a median magnitude of $G \approx 18.8$. The celestial reference frame of *Gaia* EDR3 was aligned toward ICRF3 within $\pm 10 \mu\text{as}$ in orientation at epoch 2016.0 and with a spin of less than $\pm 10 \mu\text{as yr}^{-1}$, both values at magnitude $G = 19$ (Gaia Collaboration 2021a).

The calibration processing in *Gaia* is separated into an optically faint and an optically bright part (where $G < 13$ mag), and therefore the bright fraction of the data set needs to be verified as well. Since the extragalactic objects are mostly optically faint (for DR2, all are fainter than $G = 13$ mag and 99.9% are fainter than $G = 16$ mag), the bright *Gaia* reference frame was examined with a different method. In Lindgren et al. (2018) the orientation of the bright fraction of DR2 is verified at a level of ± 0.4 milliarcseconds (mas) per axis at epoch $T = 2015.5$ by using positions and proper motions of about 20 radio stars found in the literature. The spin of the bright fraction was determined from stellar proper motion differences between DR2 and the *Tycho-Gaia* astrometric solution (TGAS; Lindgren et al. 2016) in DR1 (Gaia Collaboration 2016a) for 88 091 objects in the HIPPARCOS (van Leeuwen 2007; ESA 1997) subset of the TGAS. A significant spin of $\sim 0.15 \text{ mas yr}^{-1}$ is found. It is a result of uncalibrated instrumental effects, which will be resolved in future *Gaia* data releases (Lindgren 2020a). However, the parameters still have to be verified. In future data releases, the comparison to the HIPPARCOS data set will no longer be sufficiently accurate (Lindgren 2020a). It is suggested that VLBI observations of optically bright radio stars can be utilized for the link in both orientation and spin instead. Accordingly, an algorithm was published by Lindgren (2020a,b) that uses positions, proper motions, and parallaxes of

stars from VLBI and *Gaia* to derive the six rotation parameters. Three parameters each represent the orientation and spin about the three coordinate axes. In addition, radial velocities (needed for the rotation parameter adjustment) were taken from SIMBAD Astronomical Database (Wenger et al. 2000) whenever possible, as was done for 53 HIPPARCOS sources in DR2 (Lindgren et al. 2018). The setup also allows the inclusion of single positional measurements at one epoch or proper motion measurements without absolute positions. The algorithm was tested in Lindgren (2020a) on a sample of 41 stars found in the literature. However, only the 26 best-fitting stars were included in the final solution. The orientation offset is determined to be $(\epsilon_x, \epsilon_y, \epsilon_z) = (-0.019, +1.304, +0.553) \pm (0.158, 0.349, 0.135)$ mas, thus revealing that the offsets around the Y and Z axes are significant. The high uncertainty for the Y component results from the nonoptimal spatial distribution of the more recent VLBI observations. The spin of the DR2 bright fraction is determined to be $(\omega_x, \omega_y, \omega_z) = (-0.068, -0.051, -0.014) \pm (0.052, 0.045, 0.066)$ mas yr^{-1} relative to the VLBI reference frame (Lindgren 2020b) and is thus not significant. Similar results for the spin parameters are independently obtained by Brandt (2018).

These results are not as accurate as desired, given that the expected uncertainties for bright objects with $G \leq 13$ mag in the final *Gaia* data release will be less than $7.7 \mu\text{as}$ for positions and $5.4 \mu\text{as yr}^{-1}$ for proper motions according to de Bruijne et al. (2014). First, the major limitation of using VLBI observations of radio stars is their sparseness both in time and sky distribution. Second, many stars are located in multi-star systems, which requires the modeling of nonlinear motions. Third, binaries with separations of less than 100 mas are not resolved by *Gaia* and results refer to the photocenter (Lindgren et al. 2018), whereas they are resolved by VLBI and multiple components are detected. Fourth, radio-optical offsets of the observed emission of the stars should be considered, as the radio emission might not stem from the same position as the optical emission (Andrei et al. 1995). Because of these limitations, more radio observations of suitable optically bright stars are needed to reach the desired level of accuracy for a successful verification (Lindgren 2020a).

Most suitable stars are faint at radio frequencies, and only a few can be directly measured in absolute astrometry mode by VLBI as done for extragalactic objects in the ICRF (Titov et al. 2020). For this reason, phase-referencing as a relative observing method is commonly used for those faint targets (Wrobel et al. 2000). In this technique, a bright primary calibrator is alternately observed with the weak target. The phases from which source positions are derived can thus be determined for the bright object with a good signal-to-noise ratio (S/N) and transferred to the weak object. Thereby, precise positions of the weak objects can be determined relative to the bright objects (Reid & Honma 2014). If source positions from ICRF3 are used for the calibrators, the derived positions of the radio-weak targets are also those of the ICRF3. Furthermore, if the calibrator position improves in the future (e.g., through another realization of the ICRF), the position of the target will also improve.

This paper reports on the homogenization of data from the existing analysis of Lindgren (2020a). This homogenization was carried out by referencing the model positions of the stars to a common reference frame, obtaining a realistic error budget estimation for absolute positions from phase-referencing, and using new observations of stars in radio frequencies to enhance the verification of the *Gaia* bright reference frame. For the new observations, we selected 46 known radio stars from the literature and conducted a survey with the Very Long Baseline Array

¹ <https://mars.nasa.gov/mro/mission/timeline/mtapproach/approachopticalnav/>

(VLBA) to see which of them would be suitable for further astrometric measurements. The original purpose of the observations was to determine the peak intensities of the stars and calibrators in order to adjust on-source time for a high S/N in subsequent observations. While we report such peak intensities in the following, we also make use of the star positions derived from this short experiment to enhance the estimates of rotation parameters between the *Gaia* and ICRF3 S/X frames in various test scenarios.

Section 2 describes the effort to homogenize the historical data and gives information about the observational setup, processing, and results of the new observations. The star position differences from phase-referencing to multiple calibrators as well as the position differences between the barycenter and the center of luminosity for unresolved binaries as seen by *Gaia* are examined. In Sect. 3 the mathematical tools for the fit of the rotation parameters and the evaluation of the iterative results are given. Realistic uncertainty estimates for the absolute positions of stars from phase-referencing are also derived. In Sect. 4 various rotation parameter solutions are shown using *Gaia* DR2 and *Gaia* EDR3 data. In Sect. 5 we discuss the results, and Sect. 6 provides conclusions and an outlook. In the following, the abbreviation $\alpha^* = \alpha \cdot \cos(\delta)$ for the right ascension coordinate and a similar one for its uncertainty are used.

2. Processing of historical and new VLBI data

Lindgren (2020a) provides a determination of rotation parameters between the *Gaia* bright frame and the ICRF3 based on the collection of radio star positions, proper motions, and parallaxes provided in his Table 1. We evaluated the list and extended it with star positions from dedicated observations in January 2020. Using the *Gaia* identifier in Table 1 below, the respective *Gaia* data can be obtained from the *Gaia* archive directly, and therefore the data are not presented here.

2.1. Homogenization of historical data

As a first step, we evaluated the data in Table 1 of Lindgren (2020a). As mentioned by Lindgren (2020a), not all listed calibrator (and thus star) positions were transferred to ICRF3, some being left in the original frame. As this could result in a bias in the rotation parameters, we made efforts to transfer all such positions to ICRF3. Furthermore, it was found that the uncertainties of the star positions that were not transferred to ICRF3 did not take into account the uncertainties of the calibrator positions.

Not all original publications clearly indicate the calibrator positions used. If not found in the publication or in a cited catalog, the positions from .vex files or, if missing, from the .crd files in the VLBA observing archive² were collected in order to obtain the calibrator positions most likely used. For some publications only the observed fields were given, but it was possible to connect each star to a field and then to identify the calibrator used by cross-referencing some of the tables in the respective publications. Thus, some assumptions were made, and cross-checks with the VLBA observation archive, where metadata of the observation sessions are stored, were performed. We assume that if the calibrator positions would have been changed after the scheduling or .vex file creation, it would have been mentioned in the respective publication. For one publication contradictory information was sorted out with the help of the main author. In

all cases, the calibrator positions were given with a sufficient level of accuracy.

All original calibrator positions were identified and the differences to the ICRF3 positions were determined. They are listed in Table E.1. With this information, all star positions could be transformed to ICRF3 by applying the shifts Δ_α and Δ_δ between the original calibrator position α_{original} and δ_{original} and the ICRF3 S/X catalog position. The ICRF3 catalog position uncertainties were applied as calibrator position uncertainties $\sigma_{\alpha, \text{CRF}}$ or $\sigma_{\delta, \text{CRF}}$ to the star position uncertainties. All star positions thereby have a consistent error budget. For S Per, the calibrator position and uncertainty from the rfc_2018b catalog (Petrov 2018) were taken, as the calibrator used is not present in ICRF3. It is indicated in Table E.1. As shown in Lunz et al. (2019), the rfc_2018b and ICRF3 S/X are aligned within about 50 μs in orientation, which is acceptable at the current stage of analysis, considering the error level involved (see below). It is assumed that for the stars from references 3, 5, 14, and 17 in Table 1 of Lindgren (2020a) the model positions were already transformed to ICRF3, and the calibrator uncertainties from ICRF3 were applied, as stated in the publication. Furthermore, the two data entries for the star HD 283572 are based upon the same observational data but different calibration strategies (Galli et al. 2018); therefore, they are highly correlated³.

2.2. New one-epoch observations, data analysis, and results

In order to obtain a high probability of successful detections, it was decided to prioritize the re-observation of already known radio stars rather than testing continuum observations at radio frequencies of stars that have not yet been observed by VLBI on intercontinental baselines. This will also make it possible to refine the proper motions and parallaxes for stars within a short time by combining the data already available in the archive.

In Lunz et al. (2020) we made a literature search for stars that have been observed in radio continuum in the past and which are probably suitable for the radio-optical link. Further information on the selection process of stars and calibrators as well as the observation planning can be found in Appendix A. Both the primary calibrators, P1, and the secondary calibrators, S1 and S2, were selected, with preference given to calibrators already employed in previous observations from the literature. If in previous observations of a star different primary calibrators were used regularly, two primary calibrators P1 and P2 were chosen to see if one of them was more suitable for current observations. The secondary calibrators were not used for any corrections of the star positions in this work but only for the determination of their peak intensities for better planning of follow-up observations. The sets of stars, calibrators, and the references can be found in Table 1. To be able to connect to phase-referencing results of historical data, the stars were observed at the same frequency bands (X or C band) that were employed in previous observations.

The project was split into three experiments as shown in Table E.2, so that it was possible to observe the stars within only 14 h of VLBA observing time of the United States Naval Observatory (USNO) time-share agreement, while still getting a sufficient uv-coverage. The schedule for each star consisted of three blocks, where in each block the antennas observed the primary calibrator for 30 s, the target star for 100 s, and again the primary calibrator for 30 s. The time intervals were chosen

² www.vlba.nrao.edu/astro/VOBS/astronomy/

³ Both data entries were used for this work to be consistent with Lindgren (2020a).

Table 1. Calibrators, observation setup, and metadata for the 46 radio stars observed with the VLBA.

Star	Type	<i>Gaia</i> DR2 match	Phase-referencing calibrator		Secondary calibrator		Exp	Freq	Ref.
			<i>P1</i>	<i>P2</i>	<i>S1</i>	<i>S2</i>			
UV Psc	bL*	2576772264960362112	J0121+0422	...	J0110+0714	J0105+0600	A, C	X	1
HD 8357	XB*	2566277181659646208	J0121+0422	...	J0110+0714	J0130+0842	A, C	X	1
LS I +61 303	HXB	465645515129855872	J0244+6228	...	J0306+6243	...	A, C	X	2, 3
RZ Cas	AI*	541801332594262912	J0243+7120	...	J0319+6949	...	A, C	X	1
bet Per	AI*	239863001382455424	J0313+4120	...	J0310+3814	...	A	X	2, 3
UX Ari	RS*	118986060277836160	J0316+2733 ⁽¹⁾	J0329+2756	A	X	2, 3
HD 22468 ⁽²⁾	RS*	3263936692671872384	J0339-0146	...	J0337+0137	...	A	X	2, 3
HD 283447	TT*	163184366130809984	J0408+3032	J0403+2600	J0421+2606 ⁽¹⁾	...	A	C	4
B Per	SB*	270632486391536512	J0359+5057	...	J0413+5250	...	A	X	1
V410 Tau	TT*	164518589131083136	J0429+2724	...	J0421+2606 ⁽¹⁾	J0433+2905	A	C	5, 3
HD 283572	TT*	164536250037820160	J0429+2724	...	J0421+2606 ⁽¹⁾	J0433+2905	A	X	6
T Tau Sb	TT*	48192969034959232	J0428+1732	...	J0423+2108	...	A	C	7, 3
HD 283641	TT*	152104381299305600	J0429+2724	...	J0421+2606 ⁽¹⁾	J0433+2905	A	C	5, 3
CoKu HP Tau G2	TT*	145213192171159552	J0438+2153	J0426+2350	A	C	8
V1961 Ori	Or*	3209424108758593408	J0529-0519	...	J0541-0541	...	A	C	9, 3
Brun 334	pr*	3017270879709003520	J0529-0519	...	J0541-0541	...	A	C	9, 3
TYC 5346-538-1	Star	3015742318025842944	J0542-0913	...	J0541-0541	...	A	C	9, 3
HD 290862	Star	3219148872492984192	J0541-0211 ⁽¹⁾	...	J0552+0313	...	A	C	9, 3
SV Cam	AI*	1143477013259041920	J0626+8202	...	J0637+8125	...	A, B	X	1
R CMa	AI*	3030977013710528768	J0721-1530	...	J0725-1904	...	A, B	X	1
54 Cam	RS*	1081565094046074624	J0811+5714	...	J0752+5808	...	B	X	1
TY Pyx	RS*	5648046341168575616	J0900-2808	...	J0854-2540	...	B	X	1
XY UMa	RS*	1023682919309621632	J0902+5402	...	J0903+5151	...	B	X	1
IL Hya	RS*	5674681804189819648	J0923-2135	...	J0921-2618	...	B	X	1
HU Vir	RS*	3582095053777917952	J1216-1033	...	J1204-0710	...	B	X	1
DK Dra	RS*	1690218825255945216	J1220+7105	...	J1243+7442	...	B	X	1
RS CVn	AI*	1474194339773131648	J1308+3546	...	J1317+3425	...	B	X	1
BH CVn	RS*	1475118788534734592	J1324+3622	J1340+3754	J1322+3912	...	B	X	2, 3
RV Lib	RS*	6285122413593372032	J1436-1846	...	J1432-1801	...	B	X	1
del Lib	AI*	6332277920392457472	J1510-0843 ⁽¹⁾	J1456-0617	J1512-0905	...	B, C	X	1
AG Dra	Sy*	1642955252784454144	J1623+6624	...	J1604+6722 ⁽¹⁾	...	B, C	X	1
σ^2 CrB	RS*	1328866562170960512	J1613+3412	...	J1558+3323	...	B, C	X	2, 3
Haro 1-6	TT*	6049142032584969088	J1633-2557	...	J1625-2527	...	C	C	10, 3
DoAr 51	TT*	6047570826172040960	J1633-2557	...	J1625-2527	...	C	C	10, 3
WW Dra	RS*	1624551008683167616	J1635+5955	...	J1645+6330	...	C	X	1
Z Her	RS*	4501439984674494080	J1756+1535	...	J1758+1429	...	C	X	1
HD 226868	HXB	2059383668236814720	J1953+3537	...	J1957+3338	...	C	X	2, 3
HD 199178	Ro*	2162964329341318656	J2102+4702	...	J2114+4634	...	C	X	2, 3
ER Vul	Ae*	1845206534070618624	J2114+2832	...	J2105+2920 ⁽¹⁾	...	C	X	1
SS Cyg	DN*	1972957892448494592	J2136+4301	...	J2153+4322	...	C	X	11
RT Lac	RS*	1961028607902617216	J2153+4322	J2202+4216	J2207+4316 ⁽¹⁾	...	C	X	1
AR Lac	RS*	1962909425622345728	J2153+4322	J2202+4216	J2207+4316 ⁽¹⁾	...	C	X	2, 3
IM Peg	RS*	2829193299742131328	J2253+1608	...	J2253+1942	...	C	X	2, 3
SZ Psc	RS*	2658507622907361536	J2311+0205	J2320+0513	C	X	1
lam And	RS*	1939115478596951296	J2322+4445	...	J2354+4553	...	C	X	1
HD 224085	RS*	2855095251072482432	J2347+2719	...	J2352+3030	...	C	X	1

Notes. The columns indicate the star names and types as listed in the SIMBAD database (Wenger et al. 2000), their *Gaia* DR2 match and the respective calibrators that were observed. In order to be able to distinguish the calibrators better in future work, they were also assigned variables – *P1*, *P2*, *S1*, and *S2*. For each star, the experiment(s) (see Table E.2), the frequency band, and the reference providing the a priori position used for scheduling are given as well. In the case that two references are given, the first one describes the original data and the second one points to improved data as given in the respective reference. In this case the improved data were used. An ellipsis (...) indicates the omission of an entry. ⁽¹⁾Not in ICRF3. The position in rfc_2018b (given in the format of (α , δ)) is (49.120 883 046°±0.36 mas, 27.552 263 194°±0.45 mas) for J0316+2733, (65.263 952 933°±0.37 mas, 26.110 132 133°±0.48 mas) for J0421+2606, (85.340 401 167°±0.15 mas, -2.185 662 947°±0.29 mas) for J0541-0211, (227.727 671 113°±0.21 mas, -8.722 588 583°±0.46 mas) for J1510-0843, (241.192 478 767°±1.96 mas, 67.371 391 931°±0.66 mas) for J1604+6722, (316.431 623 725°±0.67 mas, 29.347 996 394°±0.77 mas) for J2105+2920, (331.789 686 825°±0.23 mas, 43.274 276 806°±0.28 mas) for J2207+4316. ⁽²⁾Also known as HR 1099.

References. (1) Boboltz et al. (2007); (2) Lestrade et al. (1999); (3) Lindgren (2020a); (4) Torres et al. (2012); (5) Galli et al. (2018); (6) Torres et al. (2007); (7) Loinard et al. (2007); (8) Torres et al. (2009); (9) Kounkel et al. (2017); (10) Ortiz-León et al. (2017b); (11) Miller-Jones et al. (2013).

to not lose phase-coherence between the scans of the primary calibrator at the given frequencies and considering the target-calibrator separations (Martí-Vidal et al. 2010, 2011). The three observing blocks for each star were distributed over one or two of the three experiments as listed for each star in Table 1. In one of the blocks, the secondary calibrators were observed with one 30 s scan between the respective target and primary calibrator scans. Within an experiment, frequency setups were depending on the observed star. The center frequencies were 8.11225 GHz for observations in the X band and 4.61175 GHz for the C band. Four subbands with a bandwidth of 128 MHz each were used. Dual-polarization observations were recorded with a total data rate of 4 Gbit s⁻¹. With this setup, stars as faint as 1 mJy beam⁻¹ can be detected. For each experiment additional observations to a known bright compact source were scheduled, which are needed for instrumental calibrations like bandpass calibration and global fringe fitting. Two geodetic blocks of 30 min length each containing observations to bright radio sources at various elevations were included in each experiment at the end of the first third and the second third of the scheduled time slot, to allow for atmospheric corrections using group-delays according to Mioduszewski (2009). The data were correlated at the VLBA correlator in Socorro, New Mexico (USA).

The data were processed using the NRAO Astronomical Image Processing System (AIPS; Greisen 2003) as outlined in the AIPS cookbook⁴ and with the help of ParselTongue (Kettenis et al. 2006). In the X band, strong radio frequency interference (RFI) occurred at the Pie Town antenna, and in addition the observations collected by the antenna had very low S/N. We obtained better results after flagging the antenna entirely. In the C band, RFI occurred at the Brewster antenna and the respective subband (IF 1 at 4.6118 GHz in AIPS) was flagged.

The amplitude calibration was based on Walker (2014). The a priori Earth Orientation Parameters were corrected using the final series from the USNO. Then the dispersive delay from the ionosphere was removed utilizing global maps of total electron content derived from GPS observables and provided by the Jet Propulsion Laboratory (JPL). After the purely geometric parallactic angle correction was applied, the digital sampling correction to amplitudes was carried out. In the next step, instrumental delays and phases were corrected. Pulse-calibration information was used except for antennas with ambiguities in those data. For those antennas the corrections were done manually using the known bright compact radio source J0359+5057 in experiment UL005A, J0927+3902 in experiment UL005B, J2253+1608 in experiment UL005C in the X band, and J1927+7358 in experiment UL005C in the C band. Bandpass calibration was then performed, auto-correlations were calibrated to be unity, and a priori amplitude calibration was applied using system temperature and gain curve tables. Atmospheric opacity correction was negligible at the given frequencies. Multiband delays for the observations of the geodetic blocks were produced and used to correct for elevation- and time-dependent delay errors for each antenna, as described in Mioduszewski (2009), by interpolation over all scans. The secondary calibrators are in principle used to calculate residual phase gradients between the primary calibrator and the secondary calibrator. With this additional information, the correction of the target positions can be improved using the task ATMCA in AIPS (Fomalont & Kogan 2005). However, it was not possible to employ this feature for our observations since the secondary calibrators were only scheduled in one of the three

phase-referencing blocks in order to obtain their peak intensities for follow-on observations, as noted above.

A final fringe fit of each phase-referencing calibrator was made, and corrections were applied to the respective calibrator itself as well as to its associated secondary calibrators and target star. If an object was observed in multiple experiments, its data were combined after the instrumental calibrations. In all fringe fits the calibrators were assumed to be point sources, as was done in the geodetic VLBI analysis conducted for the creation of the ICRF3. If a star was observed by using two phase-referencing calibrators, the fringe fit of the calibrator data and subsequent steps were repeated for each of the calibrators.

From these data, CLEANed images (Högbom 1974; Clark 1980) with a cell size of 0.2 mas and natural weighting (robust = 5) were produced in AIPS from which positions were derived using the task JMFIT. This task fits two-dimensional Gaussians to a given area including the source in the image. The position uncertainty resulting from this task is based on the expected theoretical precision of the interferometer and the RMS noise of the image.

An independent comparison was done with the MODELFIT task in the Caltech DIFMAP imaging package (Shepherd 1997)⁵. This task determines Gaussian model parameters of the radio source from the visibility data directly instead of from the image. The model can consist of multiple components. The uncertainty σ_{random} of a model component position was calculated from the beam shape and RMS noise of the image based on formulas for elliptical Gaussians in Condon (1997).

The evaluation of the differences in position of a star derived with both MODELFIT in DIFMAP and JMFIT in AIPS improved the reliability in the detection of faint stars and provided additional insights into the absolute position uncertainties from VLBI observations at individual epochs. We detected 32 out of the 46 observed stars with a dynamic range⁶ of 5 or higher. Details on the calculation of the peak intensities are given in Appendix B. Peak intensities for the 32 detected stars and calibrators are listed in Table B.1. The stars that could not be detected were HD 283641, V1961 Ori, HD 290862, R CMa, XY UMa, RV Lib, AG Dra, WW Dra, HD 226868, ER Vul, RT Lac, lam And, Z Her, and TY Pyx. Three of the stars (HD 283447, DoAr 51, and UX Ari) are close binaries, and the identification of their individual Aa and Ab components is described in Appendix C.

We find that MODELFIT can be more robust to find the position of the centroid of emission if structure or multiple close components are present, which is why its results are used in the following analysis. Star coordinates are listed in Table E.3 as $\alpha(t)$ and $\delta(t)$ along with their uncertainties $\sigma_{\alpha^*,\text{random}}$ and $\sigma_{\delta,\text{random}}$. The epochs of observation t are displayed with five digits after the decimal point of the Julian year to represent 6 min time difference. This higher precision compared to information in other publications such as Lindegren (2020a) is needed, because star HD 224085 in our list has a proper motion of approximately 577 mas yr⁻¹ according to literature. Such a proper motion translates to a position error of about 0.007 mas over the quoted

⁵ We corrected the u , v , w terms of the target stars to match the position of the brightest peak in the images created from the uncorrected data by using task UVFIX in AIPS. This allowed all channels of each subband to be combined, which is needed for DIFMAP, without loss of S/N due to potential bandwidth smearing in case the a priori position of the target star deviated from the approximate positions used for correlation by more than several tens of mas.

⁶ Dynamic range is defined as the ratio of the peak intensity to the image noise level.

⁴ www.aips.nrao.edu/CookHTML/CookBook.html

6-min time accuracy, which is acceptable. The three scans of this star were conducted within a time interval of 23 min in order to prevent significant smearing effects. The positions determined from the analysis of the single epoch observations were corrected for the influence of parallax to obtain positions referenced to the solar system barycenter that are comparable to those in the *Gaia* data releases. In addition, the influence of the Römer delay (geometrical delay associated with the observer's motion around the Solar System barycenter) was corrected in order to obtain the barycentric time of light arrival, as explained in Appendix A of [Lindgren \(2020a\)](#). For these reductions we derived the barycentric coordinates of the Earth center at the time of observation from the DE 421 ephemeris ([Folkner et al. 2009](#)) using the VieVS@GFZ VLBI software developed by the German Research Centre for Geosciences (GFZ). For the investigation of the *Gaia* DR2 data set, the *Gaia* parallax was applied to all stars, as the VLBI parallax is not available for all objects (for example, for the stars in [Boboltz et al. 2007](#)), and a unified result was aimed for. The parallaxes of *Gaia* DR2 are known to be biased by a few tens of μas ([Arenou et al. 2018](#)). For faint quasars an offset of -0.03 mas was determined by [Lindgren et al. \(2018\)](#), but for brighter objects this parameter was determined to be larger. A variety of studies examining this topic by using different sets of stars and methods already exist ([Riess et al. 2018](#); [Schönrich et al. 2019](#); [Zinn et al. 2019](#)). Following [Lindgren \(2020a\)](#), a parallax offset of -0.05 mas was used to keep results comparable. In the last columns of Table E.3, the calculated Römer delay $Roe(t)$ and the shifts to mitigate the parallax effect $\Delta\alpha(t)$ and $\Delta\delta(t)$ at the epoch of observation t , both using the *Gaia* DR2 parallax, are listed along with the radial velocity v_r from SIMBAD, which is needed for the transformation of the *Gaia* results to the VLBI epoch in the rotation parameter adjustment (see below). For *Gaia* EDR3, the parallax correction is not static and a python implementation calculating the bias function provided in [Lindgren et al. \(2021a\)](#) was used instead. Corrections $\Delta\alpha(t)$ and $\Delta\delta(t)$ in Table E.3 are thus slightly different for *Gaia* DR2 and *Gaia* EDR3.

By using the method of phase-referencing to calibrator positions in the ICRF3, the resulting positions of the stars refer to the ICRF3. For those calibrators that are not part of ICRF3, positions from catalog rfc_2018b were used. This should not introduce position inconsistencies since the rfc_2018b catalog is reasonably well aligned with the ICRF3, as noted above. In this work, the effect of galactocentric acceleration on the calibrator positions in ICRF3, and thus on the star positions and proper motions, was ignored. This effect would show up as a tiny but systematic global dipole pattern (with an amplitude of about $5 \mu\text{as yr}^{-1}$) in the proper motions of the stars and it would be pointing toward the Galactic center ([Titov et al. 2011](#); [Xu et al. 2012](#); [Titov & Krásná 2018](#); [MacMillan et al. 2019](#)). Only with *Gaia* EDR3 the *Gaia* internal systematics are small enough to detect this effect ([Gaia Collaboration 2021b](#)). At the current level of accuracy (see below), this effect was considered negligible and was not accounted for. An investigation of its impact is deferred to a later publication.

2.3. Multiple phase-referencing calibrators

Seven of the detected target stars, UX Ari, HD 283447, CoKu HP Tau G2, BH CVn, del Lib, AR Lac, and SZ Psc, were observed along with two different primary calibrators within the same respective observing block as indicated in Table 1. The pattern was $P1$ - $P2$ -star- $P1$ - $P2$. Therefore, the star positions relative to $P1$ and $P2$ are highly correlated in terms of error sources

Table 2. Difference $\Delta\alpha^*$ and $\Delta\delta$ in the absolute positions of seven stars when phase-referenced to two different primary calibrators.

Name	$\Delta\alpha^*$	$\sigma_{\Delta\alpha^*,\text{CRF}}$	$\Delta\delta$	$\sigma_{\Delta\delta,\text{CRF}}$
UX Ari Aa	0.33	0.34	1.18	0.46
UX Ari Ab	0.33	0.34	1.12	0.46
HD 283447 Aa	-0.21	0.24	-1.55	0.43
HD 283447 Ab	-0.20	0.24	-1.66	0.43
CoKu HP Tau G2	-0.45	0.14	0.12	0.24
BH CVn	0.63	0.21	1.45	0.33
del Lib	0.80	0.25	-1.43	0.46
AR Lac	0.20	0.10	-0.26	0.12
SZ Psc	-0.29	0.38	-0.49	0.86
RMS	0.47	0.26	1.08	0.47

Notes. Uncertainties $\sigma_{\Delta\alpha^*,\text{CRF}}$ and $\sigma_{\Delta\delta,\text{CRF}}$ were derived from the coordinate uncertainties of the primary calibrators $P1$ and $P2$ as described in Sect. 3.2. The last line indicates the RMS of the quantities, where double stars (UX Ari, HD 283447) were accounted only once in the calculations. Units are in milliarcseconds.

like earth orientation, atmosphere, and uv-coverage; however both are valid results considering an appropriate error budget. This observational setup provides the opportunity to study the accuracy of the absolute positions of these stars. The positions derived with MODELFIT in DIFMAP were obtained from the same data set once with phase referencing all objects of the group, consisting of the star and the associated calibrators, to the primary calibrator $P1$ and once with phase referencing all objects of the group to $P2$. The results are also reported in Table E.3. The differences between the positional fits to $P1$ and $P2$, $\Delta\alpha^*$ and $\Delta\delta$, are presented in Table 2. These quantities can be used to quantify potential systematic errors in the absolute star positions, which is further investigated in Sect. 3.2.

The RMS of the offsets $\Delta\alpha^*$ and $\Delta\delta$ is 0.47 mas in α^* and 1.08 mas in δ . For comparison, the RMS of the standard deviations of the catalog positions of the calibrators $\sigma_{\Delta\alpha^*,\text{CRF}}$ and $\sigma_{\Delta\delta,\text{CRF}}$ is 0.26 mas and 0.47 mas, respectively, which is a factor of 2 smaller than the RMS of the offsets. The RMS of the offsets in the α direction is half that in the δ direction. This could be due to the poor uv-coverage of our observations in the δ direction due to network geometry, as indicated by the beam sizes, and the short observation time span for most objects. For double stars only one component was considered for these calculations in order not to bias the results. For both UX Ari and del Lib, one of the calibrators is not part of the ICRF3, and thus its position and uncertainty were taken from the rfc_2018b catalog. However, the offsets for these two stars are not significantly different than those for the other stars and there seems to be no impact at the current level of precision. The offsets of the respective other primary and secondary calibrators observed along with the stars, as listed in Table 1, do not differ significantly from those of the stars.

The calibrator position from phase-referencing experiments best matches the ICRF3 catalog position if the radio source is compact. [Xu et al. \(2019a\)](#) examined 3417 celestial reference frame radio sources in terms of source structure effects in closure phase and amplitude signals over their whole observation history. They introduce the closure amplitude root mean square (CARMS). This quantity represents the lower boundary of structure effects that can be detected in the data. A CARMS value above 0.3 indicates a radio source with significant structure.

The CARMS values of Xu et al. (2019a) based on basic-noise weighting are used to verify the compactness of the primary calibrators. The values for our calibrators were confirmed by the closure statistics computed from the phase-referencing data itself. The calibrators chosen in the older historical observations, $P2$ (except for delLib, where both calibrators $P1$ and $P2$ are new), are usually very bright but have significant structure, whereas the other calibrators, $P1$, were chosen because they are more compact. However, the latter are farther away in most cases. More work has to be conducted in order to better understand which calibrator should be chosen for future observations. Surely the decision will also depend on the availability and data quality of the single epoch data from the literature and the archive.

2.4. Unresolved binaries as seen by Gaia

As mentioned in Sect. 1, *Gaia* can only distinguish between objects more than 100 mas apart and otherwise will refer to the photocenter. In our data set three close binaries that were resolved by the VLBI observations are within this threshold at the time of observation and therefore unresolved by the *Gaia* spacecraft.

The barycenter of the stellar system can be chosen as a stable reference point for comparing the trajectory of the binary from VLBI and *Gaia*. It might however not be the same position as the photocenter of *Gaia* detections. Therefore, as an alternative, we also determined the center of luminosity, as we expect it to be closer to the photocenter observed by *Gaia* than the barycenter. Even if the binaries are located within a multiple star system, we apply the binary star model as an approximation as we detected only the emission of two components.

For HD 283447 the apparent separation between the two components of the binary system was determined to be (2.824 ± 0.070) mas in α^* and (1.975 ± 0.174) mas in δ , which is the mean value of the observations to the first and the second primary calibrators (Fig. C.1). Respective values for DoAr 51 are (-4.031 ± 0.105) mas in α^* and (-5.626 ± 0.309) mas in δ (Fig. C.2). The positions of the two best fitting Gaussian components for UX Ari differ on average by (-1.514 ± 0.030) mas in α^* and (-0.268 ± 0.076) mas in δ (Fig. C.3).

For calculation of the barycenter coordinates of a binary system, the masses of the two components, m_1 for the primary and m_2 for the secondary, are needed. For HD 283447 Aa and Ab the masses are given in Torres et al. (2012), for DoAr 51 they are given in Ortiz-León et al. (2017b) and for UX Ari they are given in Hummel et al. (2017). Then, the vector \mathbf{r}_1 between the primary star position and the barycenter is (Torres et al. 2012)

$$\mathbf{r}_1 = \frac{m_1}{m_2 + m_1} \mathbf{r}, \quad (1)$$

where \mathbf{r} is the separation between the primary and secondary star.

The center of luminosity was calculated in the same manner, but instead of the masses the luminosities of the stars were used for the calculations. For HD 283447 the optical luminosities for components Aa and Ab are given in Welty (1995) and for UX Ari, they are given in Hummel et al. (2017). For DoAr 51 we determined a factor equivalent to $\frac{m_1}{m_1 + m_2}$ from the flux ratio in Schaefer et al. (2018), assuming that both stars are equally distant, since we could not find the luminosities directly. We used the J-band flux ratio because it is the closest to the *Gaia* bands. The components in α and δ of the vector \mathbf{r}_1 , which provides the barycenter offset or luminosity center offset from the primary

star and their differences, are listed in Table 3. They are several hundreds of microarcseconds large. These offsets can be added to the position of the primary star of the binary system to obtain the absolute positions of the barycenter and center of luminosity.

The differences between the barycenter and center of luminosity positions remain similar whether using the $P1$ or the $P2$ calibrator for phase-referencing. No clear sign could be found which of the two centers match better the *Gaia* position at the VLBI epoch. Therefore, no final conclusion can be made at this point, and the center of luminosity is used in the following.

3. Analysis method

In this section the relevant tools for the rotation parameter analysis and evaluation are described.

3.1. Combined fit of rotation parameters and corrections to the Gaia astrometric models

As we apply the same algorithm as introduced in Lindegren (2020a) for simultaneously fitting the orientation and spin parameters between VLBI and *Gaia* along with adjustments to the star model of *Gaia* transformed to the VLBI epoch, we only give a short description here. We use the same terms of “orientation”, denoted $\epsilon(T) = (\epsilon_X(T), \epsilon_Y(T), \epsilon_Z(T))$ for conciseness, for the instantaneous global solid-body rotation between two reference frames about their three axes X, Y, and Z at reference epoch T , and of “spin,” denoted $\omega = (\omega_X, \omega_Y, \omega_Z)$, for the corresponding the rotation rate. Consequently, an orientation offset at epoch t can be calculated as

$$\epsilon(t) = \epsilon(T) + (t - T)\omega. \quad (2)$$

The coordinate differences from the orientation offset between two reference frames, in this case determined by VLBI and *Gaia*, are given by

$$(\alpha_{VLBI} - \alpha_{Gaia}) \cos \delta = + \epsilon_X \cos \alpha \sin \delta + \epsilon_Y \sin \alpha \sin \delta - \epsilon_Z \cos \delta, \quad (3)$$

$$\delta_{VLBI} - \delta_{Gaia} = - \epsilon_X \sin \alpha + \epsilon_Y \cos \alpha, \quad (4)$$

where the star positions determined by VLBI, α_{VLBI} and δ_{VLBI} , and the star positions determined by *Gaia*, α_{Gaia} and δ_{Gaia} , are at the same epoch t . Similar equations are used for the differences in proper motion,

$$(\mu_{\alpha_{VLBI}} - \mu_{\alpha_{Gaia}}) \cos \delta = + \omega_X \cos \alpha \sin \delta + \omega_Y \sin \alpha \sin \delta - \omega_Z \cos \delta, \quad (5)$$

$$\mu_{\delta_{VLBI}} - \mu_{\delta_{Gaia}} = - \omega_X \sin \alpha + \omega_Y \cos \alpha. \quad (6)$$

In the combined estimation of $\epsilon(T)$ and ω , written as the column vector $x = [\epsilon_X(T), \epsilon_Y(T), \epsilon_Z(T), \omega_X, \omega_Y, \omega_Z]^T$, the observables are the position, proper motion, and parallax differences, Δf_i . These quantities are determined as the differences between the observed VLBI data and the *Gaia* data set propagated to the VLBI epoch, and are available for a total of S stars. The position offsets contribute to the determination of both orientation and spin, whereas the proper motion differences contribute to the spin determination only. The results of the least squares fit are an estimate \hat{x} for the six rotation parameters between the two frames along with estimates of the five astrometric parameters for each star i (where $i = 1 \dots S$), and their full covariance matrix. The residuals v_i for the star i are calculated as the differences between the VLBI data and the predicted *Gaia* data

Table 3. Components in α and δ of the vector \mathbf{r}_1 , which provides the position of the barycenter or center of luminosity with respect to the position of the primary star for the close binary systems in UX Ari, HD 283447, and DoAr51.

	Barycenter				Center of luminosity				Difference			
	r_{1,α^*}	$\sigma_{r_{1,\alpha^*}}$	$r_{1,\delta}$	$\sigma_{r_{1,\delta}}$	r_{1,α^*}	$\sigma_{r_{1,\alpha^*}}$	$r_{1,\delta}$	$\sigma_{r_{1,\delta}}$	r_{1,α^*}	$\sigma_{r_{1,\alpha^*}}$	$r_{1,\delta}$	$\sigma_{r_{1,\delta}}$
UX Ari, <i>P1</i>	-0.707	0.020	-0.139	0.052	-0.304	0.009	-0.060	0.022	-0.403	0.022	-0.079	0.056
UX Ari, <i>P2</i>	-0.708	0.019	-0.111	0.049	-0.305	0.008	-0.048	0.021	-0.403	0.021	-0.063	0.053
HD 283447, <i>P1</i>	1.286	0.045	0.873	0.111	0.568	0.020	0.386	0.049	0.717	0.049	0.487	0.121
HD 283447, <i>P2</i>	1.283	0.045	0.924	0.113	0.567	0.020	0.408	0.050	0.716	0.050	0.515	0.123
DoAr51, <i>P1</i>	-2.003	0.052	-2.795	0.153	-2.169	0.057	-3.028	0.166	0.167	0.077	0.233	0.226

Notes. If two primary calibrators – *P1* and *P2* – were available for phase-referencing, the results from referencing to each of them are shown. The standard deviations for the components of the vector \mathbf{r}_1 , $\sigma_{r_{1,\alpha^*}}$ and $\sigma_{r_{1,\delta}}$, are based on random error (see Sect. 3.2) and variance propagation. Units are in milliarcseconds.

corrected for the rotation offset using the estimates of the rotation parameters (for more information see Lindegren 2020a). The term $Q_i/n_i = Q_i(\hat{x})/n_i$ describes the discrepancy of a star, i , for a given solution, \hat{x} , where n_i is the number of observables for the star contained in the solution (i.e., the length of the vector Δf_i). The quantity $Q_i(\hat{x})$ can be determined from the residuals v_i as

$$Q_i(\hat{x}) = v_i' D_i^{-1} v_i, \quad (7)$$

where D_i is the covariance of Δf_i . If the data fits the five-parameter astrometric model well and the uncertainties of the observables are correctly estimated, Q_i/n_i should be close to unity. We used this measure for the iterative analysis of the rotation parameters in the following way: after a first fit using all stars, the star with $\max(Q_i/n_i)$ is discarded from the data set and another fit involving only the new subset of stars is determined, then the star with $\max(Q_i/n_i)$ from the new fit is discarded as well, and so on. In the end, all possible solutions with $k = 0, 1, 2, \dots$ discarded stars are analyzed. In addition, the quantity $Q/n = \sum Q_i / \sum n_i$, is used to evaluate the improvement of the overall fit at each iteration.

3.2. Discussion on VLBI position error bounds

The positions derived in the previous sections are of two kinds, that is, the model positions from Sect. 2.1 and the single-epoch positions from Sect. 2.2. The single-epoch positions describe the star positions at a specific epoch in time. For these positions no averaging or correction for nonvisible binary companions and other disturbances could be applied. In contrast, the model positions from a fit of relative position time series to models of stellar motion (usually mean position, proper motion, and parallax) are affected by such disturbances. These would increase the uncertainty of the estimated astrometric parameters because the formal errors are usually adjusted so that the reduced χ^2 of the fit equals unity. The impact is minimized by selecting stars with a small renormalized unit weight error (RUWE) parameter (calculated from *Gaia* DR2 data; Lindegren et al. 2018), indicating that the *Gaia* data fits the five-parameter astrometric model well, and by the iterative approach, where deviating stars get rejected first. Nevertheless, the difference of the error budget for the two types of positions needs further investigation, which is given in the following.

In general, positions derived from phase-referencing measurements, as in the present study, are affected by the following five thermal or systematic errors. The first is the random error σ_{random} [thermal] due to thermal noise calculated based on

the S/N and the shape of the elliptical Gaussian fitted to the central map component (e.g., Thompson et al. 1986; Condon 1997). Mean (Median) values of 0.034 (0.026) mas in α^* and 0.087 (0.067) mas in δ are obtained from the data of this study.

The second is the celestial reference frame calibrator position uncertainty, σ_{CRF} [thermal]. The median position uncertainty in ICRF3 S/X is 0.1 mas in α and 0.2 mas in δ . The additional error due to the absolute position wander of individual calibrators, for example quantified by the Allan variance in Gattano et al. (2018), is ignored.

The third is the delay model error $\sigma_{\text{delay model}}$ [systematic] from residual ionospheric and tropospheric errors, antenna and calibrator position errors, and Earth orientation parameter errors. These mostly depend on the declination of the source and the calibrator-target separation. Pradel et al. (2006) determined that the combined error is roughly between 0.015 mas to 0.284 mas per coordinate direction for a calibrator-target separation of 1° based on a simulation without ionospheric delay uncertainty considered. The uncertainty due to residual ionospheric delay from JPL total electron content maps is below 0.1 mas.

The fourth is the source structure error $\sigma_{\text{structure}}$ [systematic] due to non-point-like and possibly varying calibrator structure. The larger the structure, the higher the effect. When modeling calibrator structure, the positions of the stars estimated in our analysis show a mean difference of -0.003 mas in α^* and 0.002 mas in δ , while the RMS of the differences is 0.019 mas in α^* and 0.035 mas in δ .

The last is the uncertainty $\sigma_{\text{phase-group}}$ [systematic] due to the difference between calibrator group- and phase-delay positions in the presence of core shift (possibly varying with time). This uncertainty was determined to be between 0.036 mas and 0.326 mas for a source with a median core shift between the S and X band of 0.44 mas (Kovalev et al. 2008) and for a variety of power-law exponents (Porcas 2009). We anticipate the impact of core shift in the C band to be smaller since this frequency lies between the S and X frequency bands. In practice, it is possible that $\sigma_{\text{phase-group}}$ is also affected by structure at S band, which impacts the S/X positions, but this is only a second order effect.

All of these effects are unique in magnitude and direction in the sky from radio sources to radio sources.

A possible way to get insights into the magnitude of unaccounted systematic errors in the single-epoch positions may be obtained by comparing absolute star positions determined by phase-referencing with respect to two different calibrators (see Sect. 2.3). In principle, that is to say, in the absence of systematic errors, the difference in the absolute positions of a star measured in such a case should be consistent with the uncertainties derived from a combination of the positions uncertainties of the two

calibrators in the ICRF3, $\sigma_{\Delta\alpha^*,\text{CRF}}$ and $\sigma_{\Delta\delta,\text{CRF}}$. Any difference larger than that reveals the presence of systematic errors. In our analysis (see Sect. 2.3 and Table 2), the RMS of the differences of the star positions, $\Delta\alpha^*$ and $\Delta\delta$, is on average twice as large as the combined calibrator uncertainties, $\sigma_{\Delta\alpha^*,\text{CRF}}$ and $\sigma_{\Delta\delta,\text{CRF}}$. Thus, our analysis is not free of systematic errors. To evaluate the magnitude of such systematic errors, we subtracted in quadrature the RMS of $\sigma_{\Delta\alpha^*,\text{CRF}}$ and $\sigma_{\Delta\delta,\text{CRF}}$, respectively, from the RMS of $\Delta\alpha^*$ and $\Delta\delta$, as $\sqrt{0.47^2 - 0.26^2} / \sqrt{2} = 0.28$ mas for α^* and $\sqrt{1.08^2 - 0.47^2} / \sqrt{2} = 0.69$ mas for δ . The errors thus determined can then be added to the thermal errors σ_{random} and σ_{CRF} to get the absolute star position uncertainties, expressed as

$$\sigma_{\alpha^*,\text{absolute}}^{\text{single epoch}} = \sqrt{\sigma_{\alpha^*,\text{random}}^2 + [\sigma_{\alpha^*,\text{CRF}} \cdot \cos(\delta)]^2 + 0.28^2} \text{ mas} \quad (8)$$

and

$$\sigma_{\delta,\text{absolute}}^{\text{single epoch}} = \sqrt{\sigma_{\delta,\text{random}}^2 + \sigma_{\delta,\text{CRF}}^2 + 0.69^2} \text{ mas}. \quad (9)$$

The values of these absolute positional uncertainties are reported in Table 4 for each of the 32 detected individual stars in addition to their random errors. The mean (median) of such values for all stars in our sample are 0.315 (0.305) mas for α^* and 0.738 (0.714) mas for δ .

In case of star positions derived from fitting models of stellar motion to multi-epoch relative positions, many systematic errors were accounted for by inflating the formal errors such that the χ^2 of the fit equals one. Such inflated errors are labeled $\sigma_{\text{model pos}}$ if the σ_{CRF} were added (as it was done for the homogenization efforts in Sect. 2.1). However, not all systematic errors can be accounted for by this method. To complete the error budget, an additional component to account for $\sigma_{\text{phase-group}}$ still needs to be applied. We found three approaches for estimating the magnitude of this uncertainty. First, the difference between group-delay position and phase-delay position determined from simulations in Porcas (2009) is 0.166 mas for a core shift of 0.440 mas between 2.3 GHz and 8.4 GHz, and in the case of an ideal source having no jet. Second, Fomalont et al. (2011) studied the difference between ICRF2 positions and positions from phase-referencing at 8.6 GHz for four compact radio sources by using the VLBA. The conclusion was that the positions in ICRF2 can be offset from the phase-referenced positions (materialized by the core of the sources) by up to 0.5 mas, with the mean offset being 0.42 mas. Dividing this value by $\sqrt{2}$ a $\sigma_{\text{phase-group}}$ magnitude of 0.30 mas per coordinate direction is obtained. Third, the trajectory of the Cassini spacecraft was observed at 8.4 GHz relative to various primary calibrators by the VLBA as well (Jones et al. 2020). From this study, $\sigma_{\text{phase-group}}$ was determined to be in the range of 0.18 mas to 0.20 mas, similar to the above values. The mean value of the three approaches is 0.21 mas. For star positions observed in the C band, the magnitude might be smaller due to the C band being in between the S- and X-band frequencies. However, this is not considered in this study. Based on our analysis, an extra noise of 0.21 mas was thus added to $\sigma_{\text{model pos}}$ to obtain a more realistic error budget for the absolute positions derived from models of stellar motions:

$$\sigma_{\alpha^*,\text{absolute}}^{\text{model}} = \sqrt{\sigma_{\alpha^*,\text{model pos}}^2 + 0.21^2} \text{ mas} \quad (10)$$

and

$$\sigma_{\delta,\text{absolute}}^{\text{model}} = \sqrt{\sigma_{\delta,\text{model pos}}^2 + 0.21^2} \text{ mas}. \quad (11)$$

The more realistic error budget for the absolute positions presented in this section must be used when comparing the two kinds of absolute positions from VLBI (single-epoch or derived from models of stellar motions) to an independent measurement system such as *Gaia*.

3.3. Metrics for evaluating the rotation parameters

To compare the iterative solutions of the rotation parameters for various scenarios s , the steadiness of the parameters can be used as a criterion for the reliability of such solutions. Three quantities were computed to this end: (i) the weighted mean (WM) of the rotation parameters, WM_s , (ii) the weighted root mean square (WRMS) of the difference between the rotation parameters at each iteration and the WM over all iterations, WRMS_s , and (iii) the mean of the parameter formal errors, ME_s . These quantities can be expressed as

$$\text{WM}_s = \frac{\sum_{k=i}^j \hat{x}_k / \sigma_k^2}{\sum_{k=i}^j 1 / \sigma_k^2}, \quad (12)$$

$$\text{WRMS}_s = \sqrt{\frac{(j-i+1) \sum_{k=i}^j [(\hat{x}_k - \text{WM}_s)^2 (1/\sigma_k^2)]}{(j-i) \sum_{k=i}^j 1/\sigma_k^2}}, \quad (13)$$

$$\text{ME}_s = \frac{\sum_{k=i}^j \sigma_k}{j-i+1}, \quad (14)$$

where \hat{x}_k is the rotation parameter of interest at iteration k and σ_k its uncertainty. Only a representative range of iterations was used to derive these quantities. The start, i , of the selected iterations was chosen so that no outliers were included, and the stop, j , was chosen to avoid having too few stars left in the sample and thereby allow us to obtain reliable estimates of the rotation parameters. For solutions without the January 2020 positions, the WM_s and WRMS_s were calculated from iterations $i = 9$ to $j = 34$, while for solutions including the January 2020 positions, iterations $i = 12$ to $j = 47$ were considered. When calculating ME_s , the last ten iterations were left out because the formal errors then tend to be larger compared to those in the range of iterations where the baseline solution is normally chosen.

If WRMS_s is two times larger than ME_s , the rotation parameter estimates are considered statistically unstable within a scenario. The significance of the difference in rotation parameters between two scenarios can be determined by a two-sample t-test with the null hypothesis that means are equal and a 5% significance level. It is assumed that the rotation parameters are normal distributed with unknown and unequal variances, which is the Behrens-Fisher problem. If the test cannot be accepted and the probability value (p-value) is smaller than the significance level, the parameter difference between two scenarios is significant.

4. Improved rotation parameters

In this section we present various iterative solutions for rotation parameters between different VLBI and *Gaia* data sets. Solution “41,DR2,Lind2020” corresponds to the solution published by Lindgren (2020a). The effects of homogenizing the complete data from Lindgren (2020a) versus *Gaia* DR2 and applying more realistic errors are shown in solution “41,DR2.” Second, the results using *Gaia* EDR3 are presented in solution “41,EDR3.” Third, the implications of the new one-epoch observations are demonstrated in solutions “55,DR2” and “55,EDR3”.

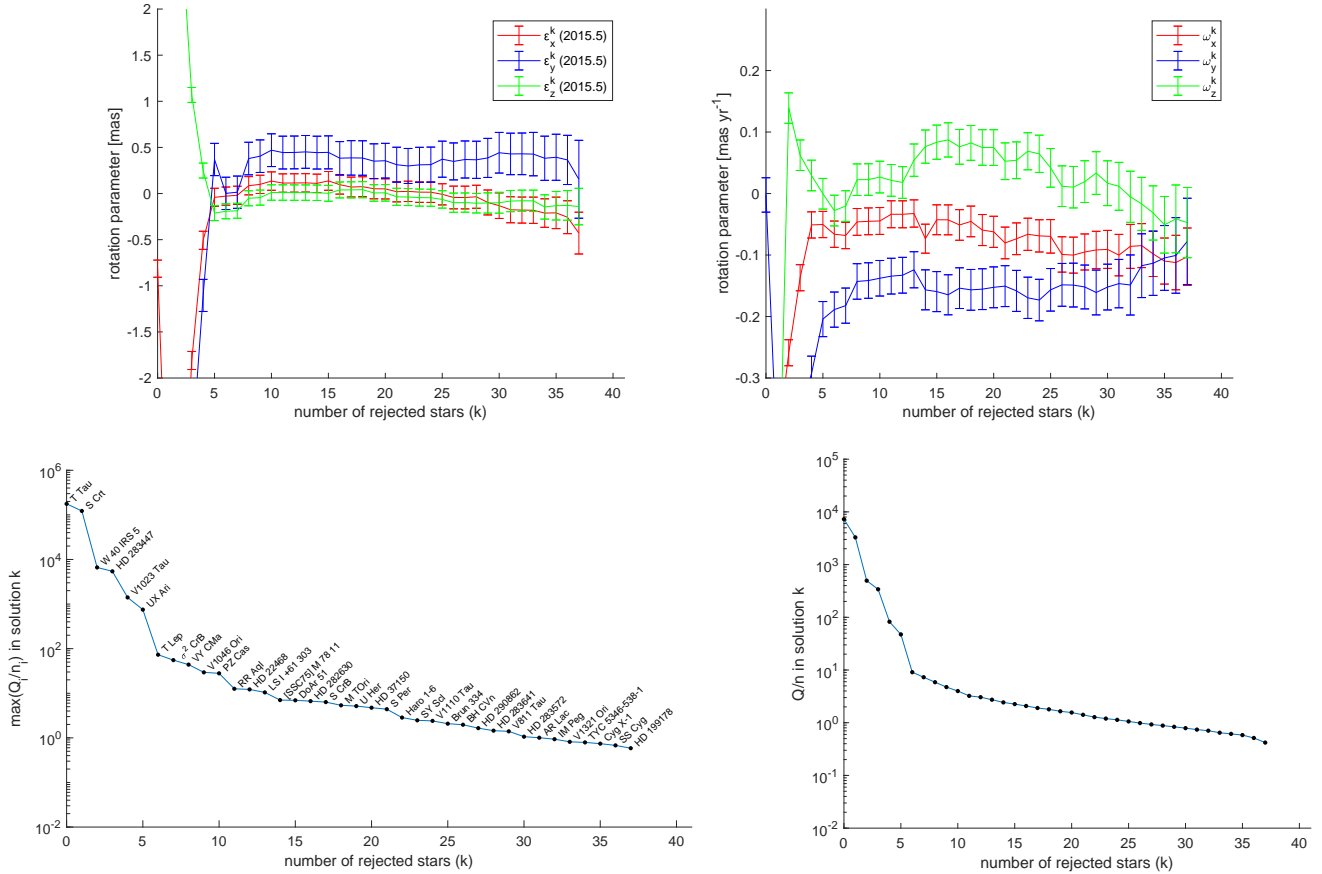


Fig. 1. Results for the homogenized Lindegren (2020a) data set 41,DR2 that includes more realistic uncertainties for the absolute VLBI star positions. The upper row shows the orientation and spin parameters for 38 different adjustment solutions, where for each adjustment solution the star with the largest (Q_i/n_i) was rejected in the following iteration. The respective (Q_i/n_i) and the star names are given in the lower-left plot. The lower-right plot represents the quality of the fit, equivalent to the χ^2 of the adjustment, the so-called Q/n .

4.1. Homogenized data set

Recalculating the rotation parameters using the homogenized data of the 41 stars from Sect. 2.1 and the more realistic errors from Sect. 3.2 yields scenario 41,DR2, which is pictured in Fig. 1. For completeness, the results for a scenario “41,DR2, $\sigma_{\text{model pos}}$ ” are provided in Appendix D. Both scenarios are based on the same values for the star positions. However, the star positions in 41,DR2 have uncertainties σ_{absolute} applied, whereas those in 41,DR2, $\sigma_{\text{model pos}}$ have only the thermal errors applied (see Sect. 3.2). The latter application is similar to the error scheme in Lindegren (2020a), but applied consistently to all stars. In total, 38 iterations were performed. In the upper two plots in Fig. 1 the results of the orientation (left) and spin (right) parameters are shown, while in the lower left plot, the $\max(Q_i/n_i)$ quantity along with the corresponding star names are given. The lower right plot gives information about the goodness of the fit, Q/n . All plots are relative to the number of rejected stars, k , in the iteration.

The homogenization and the more realistic error budget reduce the WRMS of the parameters by a factor of 2 to 4 for ϵ_y , ϵ_z , ω_x , and ω_y when compared to the original scenario 41,DR2,Lind2020 (see Table 4). On the other hand, the parameters ϵ_x and ω_z are only slightly affected. The mean formal errors $\text{ME}_{41,DR2}$ of the orientation parameters are 2.5–3.5 times those in scenario 41,DR2,Lind2020, whereas the mean formal errors of the spin parameters only increase marginally. The ratio between $\text{WRMS}_{41,DR2}$ and $\text{ME}_{41,DR2}$ is not significant for

scenario 41,DR2, whereas it was significant for all orientation parameters in scenario 41,DR2,Lind2020. The t-test shows that the reduction in ϵ_y of 0.88 mas, and ϵ_z of 0.56 mas as well as the increase in ω_y of 0.07 mas yr^{-1} are significant.

The shifted phase-referencing calibrator positions from historical positions to ICRF3 positions are mostly less than a milliarcsecond but they have a large impact on both orientation and spin parameters, given the provided data set. In addition, the improved weighting of the model star positions by applying the calibrator catalog uncertainties homogeneously for all stars, and not a mixture of error budgets as in Lindegren (2020a), influences the resulting rotation parameters as well (see Appendix D). The change in the error budget for the positions has the largest impact on the orientation parameters. This approach reduces the Q/n quantity compared to 41,DR2,Lind2020. It now decreases below unity when $k = 26$ stars are rejected, compared to $k = 33$ rejected stars for 41,DR2,Lind2020. The plots showing the evolution of the variable $\max(Q_i/n_i)$ with the number of rejected stars k indicate that the order of rejected stars is almost the same.

4.2. Gaia EDR3

Also, in Gaia EDR3 no matched ICRF3 S/X radio sources are brighter than $G = 13$ mag and optically bright radio stars are needed for the link of the bright Gaia reference frame to ICRF.

Gaia EDR3 is based on a longer observation time span than DR2, and the epoch of the catalog changed to $T = 2016.0$. Velocities are still only modeled linearly. Higher order terms or orbits

Table 4. WM, WRMS, and ME of the various rotation parameter scenarios.

Scenario		$\epsilon_X(\text{T})$	$\epsilon_Y(\text{T})$	$\epsilon_Z(\text{T})$	ω_X	ω_Y	ω_Z
41,DR2,Lind2020	WM _{41,DR2,Lind2020}	0.055	1.273	0.537	-0.047	-0.081	0.028
	WRMS _{41,DR2,Lind2020}	0.105	0.237	0.087	0.050	0.037	0.030
	ME _{41,DR2,Lind2020}	0.031	0.073	0.025	0.023	0.028	0.028
41,DR2	WM _{41,DR2}	0.038	0.391	-0.025	-0.061	-0.150	0.045
	WRMS _{41,DR2}	0.090	0.051	0.047	0.022	0.013	0.029
	ME _{41,DR2}	0.104	0.182	0.087	0.024	0.032	0.028
41,EDR3	WM _{41,EDR3}	0.204	0.221	0.067	0.024	0.050	-0.027
	WRMS _{41,EDR3}	0.094	0.129	0.079	0.016	0.015	0.014
	ME _{41,EDR3}	0.110	0.189	0.087	0.013	0.016	0.013
55,DR2	WM _{55,DR2}	0.062	0.364	-0.015	-0.067	-0.135	0.038
	WRMS _{55,DR2}	0.038	0.062	0.073	0.014	0.014	0.018
	ME _{55,DR2}	0.081	0.107	0.063	0.021	0.026	0.024
55,EDR3	WM _{55,EDR3}	0.294	0.340	0.077	0.034	0.055	-0.020
	WRMS _{55,EDR3}	0.049	0.074	0.084	0.016	0.014	0.012
	ME _{55,EDR3}	0.079	0.099	0.060	0.011	0.013	0.012

Notes. For scenarios “41” not including the January 2020 positions, iterations 9 to 34 were used for calculation, whereas for scenarios “55” including the January 2020 positions, iterations 12 to 47 were considered. For derivation of values ME_s the last 10 iterations were rejected because the formal errors of the rotation parameters increase substantially if only a few stars are available for calculation. Units are in milliarcseconds for ϵ_X , ϵ_Y , and ϵ_Z and milliarcseconds per year for ω_X , ω_Y , and ω_Z .

due to multiple star systems are neglected. Therefore, differences in proper motion of *Gaia* EDR3 and DR2 may not only be due to better sampling but also due to nonlinear motions. The red supergiant VY CMa shows very large differences between *Gaia* DR2 and EDR3. Its *Gaia* EDR3 proper motion better matches the VLBI data in Zhang et al. (2012). In addition its negative parallax of approximately -6 mas in *Gaia* DR2 disappeared. *Gaia* EDR3 was corrected for its spin offset during the *Gaia* data processing. Therefore, the adjusted rotation parameters (Fig. 2) are the orientation and residual spin of the frame as determined by VLBI. The uncertainty in the *Gaia* EDR3 spin correction is at least $0.024 \text{ mas yr}^{-1}$ per axis (Lindgren et al. 2021b).

All WM parameters change significantly in solution 41,EDR3 compared to the result for *Gaia* DR2 (see Table 4). The magnitude of the orientation parameters changed by 0.09 mas to 0.17 mas, and that of the spin parameters by 0.07 mas yr^{-1} to 0.20 mas yr^{-1} . The WRMS_{41,EDR3} is between 0.079 and 0.129 mas for the orientation parameters, corresponding to 1.0- to 2.5-fold the values for *Gaia* DR2. At the same time, their mean formal errors remain similar because the error budget for the orientation parameters is dominated by the (inflated) VLBI uncertainties. In contrast, the mean formal errors for the spin are only about 50 % of those for 41,DR2, which is expected due to smaller proper motion uncertainties in *Gaia* EDR3 compared to *Gaia* DR2 due to the longer observation time span in *Gaia* EDR3. Moreover, the WRMS_{41,EDR3} for ω_Z reduced by a factor of 2.1 and that for ω_X by a factor of 1.4.

4.3. Including the new one-epoch observations

The newly derived single-epoch star positions determined with the VLBA were inserted into the analysis. If the stars were observed relative to two different primary calibrators, both positions were employed in the adjustment. This will, if only those two positions are present, result in a WM position for the corresponding stars. For close binaries the center of luminosity was used.

Star bet Per, although successfully detected in VLBI, was not used in the adjustment. In our VLBI observations in January 2020, star bet Per was scheduled although it only had a matching object in *Gaia* DR2 with a two parameter solution (position only). It was assumed that in *Gaia* EDR3 a five parameter solution would be available for the object assumed to be bet Per due to the longer data time span and therefore presumably more observations for the parameter fit. The assumption was supported by the fact that the star was also detected by its predecessor spacecraft HIPPARCOS. However, in *Gaia* EDR3, no counterpart was found for bet Per. This position will however be useful if comparing to future *Gaia* data releases, should a counterpart with a full five-parameter solution be available for the star. In total, the observations of 55 stars in both VLBI and *Gaia* were utilized for the adjustment of the rotation parameters. There were 21 stars that had more than one entry of positions or proper motions. Eleven stars had only a position measurement and no proper motion or parallax. Three stars had only a proper motion and parallax entry but no position. The remaining stars had one position, proper motion, and parallax entry.

Having 55 stars available, 52 iterations were run, with the same rule for star rejection as in Sect. 4.1 applied. Two solutions of the frame tie, 55,DR2 and 55,EDR3, were generated. The WM, WRMS, and ME values are given in Table 4. The respective plots for *Gaia* EDR3 are shown in Fig. 3. Comparing 55,EDR3 with 41,EDR3, the MEs reduce by 30–50% for the orientation parameters, and by 10 to 20% for the spin parameters. This decrease can be explained by the increase in the volume of observations. In both orientation and spin, the MEs in *Y* decrease most but are still the largest compared to the MEs in *X* and *Z*. For 55,EDR3 the value of unity is reached for Q/n when 15 stars are still in the sample, whereas for 41,EDR3 it is 9 stars. The WRMSs decrease by 40–50% for the orientation parameters in *X* and *Y*, while they remain similar for the other rotation parameters. The WMs change significantly (by about 0.1 mas) for parameters ϵ_X and ϵ_Y .

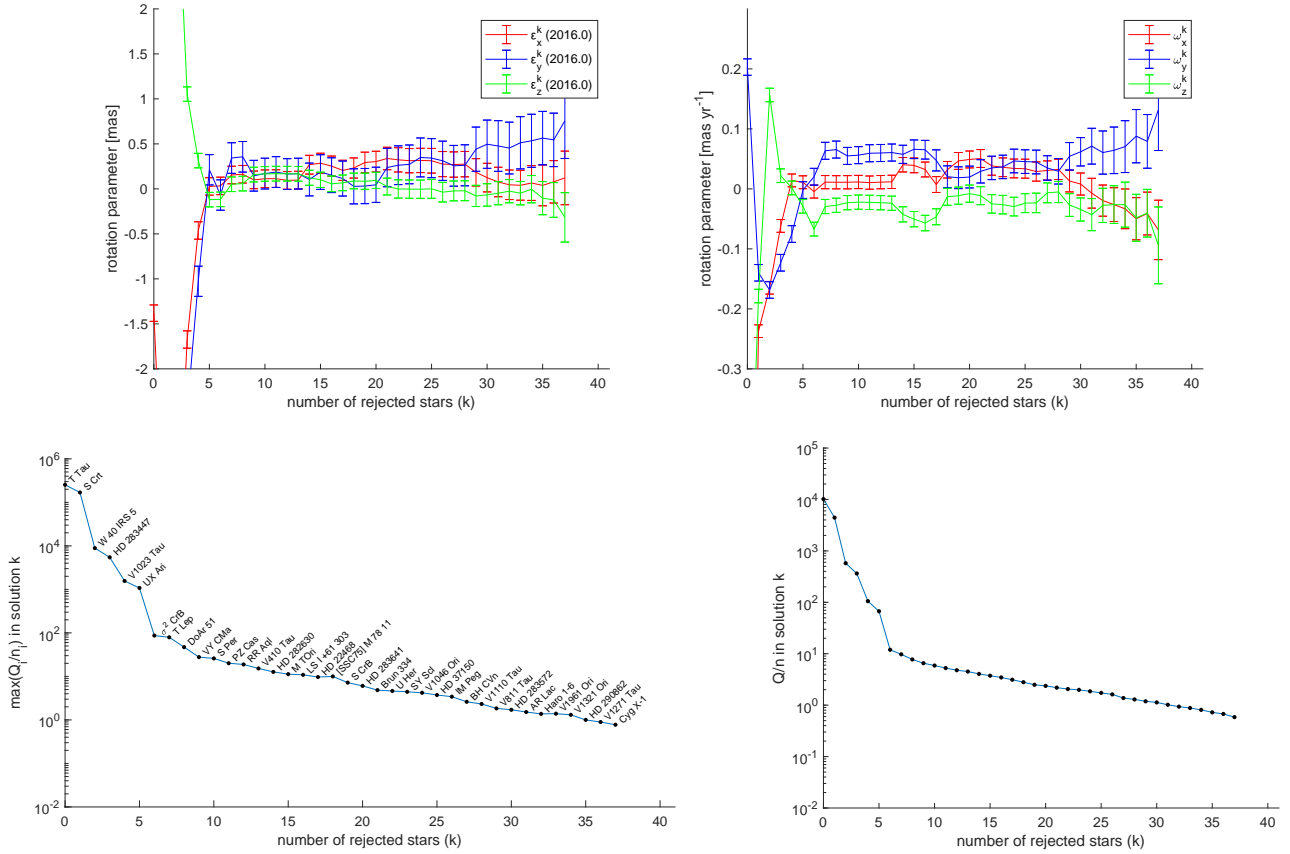


Fig. 2. Results for the homogenized Lindegren (2020a) data set 41,EDR3 that includes more realistic uncertainties for the absolute star VLBI positions. For a description of the plots, refer to Fig. 1.

The quantities change similarly when comparing 55,DR2 to 41,DR2. The MEs reduce by 20 to 40% for the orientation parameters, and by 10 to 20% for the spin parameters. The Q/n reaches unity when there are 9 more stars in the sample (plot not shown). The WRMSs vary very heterogeneously. For ϵ_X it decreases by 60%, whereas for ϵ_Y and ϵ_Z it increases by 20% and 50%, respectively. For ω_X and ω_Z the WRMS decreases by 35%, while it remains similar for ω_Y . According to the two-sample t -test introduced in Sect. 3.3, the WM changes for ϵ_Y (-0.027 mas) and ω_Y (0.015 mas yr $^{-1}$) are significant.

5. Discussion

5.1. Homogenization effect and realistic error budget

When the model positions of 29 stars were consistently referenced to the ICRF3 (scenario 41,DR2), the orientation parameters in Y and Z, and, more importantly for the frame alignment, the spin parameter in Y, were found to change significantly compared to the original scenario of Lindegren (2020a, i.e., scenario 41,DR2,Lind2020).

In this case, a spin vector with a magnitude lower than 0.1 mas yr $^{-1}$, as obtained in the baseline solution of Lindegren (2020b), cannot be reached. The homogenization of the input data showed a great improvement in reducing the jumps in the orientation and spin parameters with subsequent iterations. This is a demonstration that one needs to carefully consider the systematic errors of the VLBI positions for the weighting in the frame tie determination. The effect of homogenization stresses the benefit of revisiting historical VLBI data for the alignment of *Gaia* to ICRF3, especially because the observations of radio stars

are sparse and any systematic errors due to the use of inconsistent positions would thus likely impact the result.

In Appendix D, the results of scenario 41,DR2, $\sigma_{\text{model pos}}$ are presented. This scenario is the same as 41,DR2, but using a VLBI position error budget based only on the uncertainties from the fit of the astrometric model and the calibrator catalog position uncertainty, applied consistently to all stars. The MEs are higher for 41,DR2 compared to 41,DR2, $\sigma_{\text{model pos}}$, as expected due to the inflated VLBI uncertainties. At the same time, the WRMS values in solution 41,DR2 are no better than those in solution 41,DR2, $\sigma_{\text{model pos}}$ despite the increase in the VLBI position uncertainties – in details, the WRMS values are slightly better for ϵ_X , ϵ_Y , and ω_X (by 10% at most) but are 15–35% worse for ϵ_Z , ω_Y , and ω_Z . The number of rejected stars to obtain $Q/n = 1$, changes from 29 in 41,DR2, $\sigma_{\text{model pos}}$ to 26 in 41,DR2, a difference that can be expected just from the inflated VLBI position uncertainties in 41,DR2. In all, the differences between solutions 41,DR2, $\sigma_{\text{model pos}}$ and 41,DR2 are not that marked – the major changes happen when going from solution 41,DR2,Lind2020 to 41,DR2, $\sigma_{\text{model pos}}$. The correlation coefficients between the three orientation parameters are all above 0.5 for 41,DR2, $\sigma_{\text{model pos}}$, whereas they are reduced by 0.1–0.2 for 41,DR2. These reduced correlations may explain the significant change in ϵ_X (0.038 in scenario 41,DR2 vs. -0.152 in scenario 41,DR2, $\sigma_{\text{model pos}}$), whereas all other parameters are similar.

5.2. Alignment of *Gaia* DR2 and adding new one-epoch positions

Given the variability of our iteration solutions, the question arises as to how a baseline solution (i.e., a selected iteration

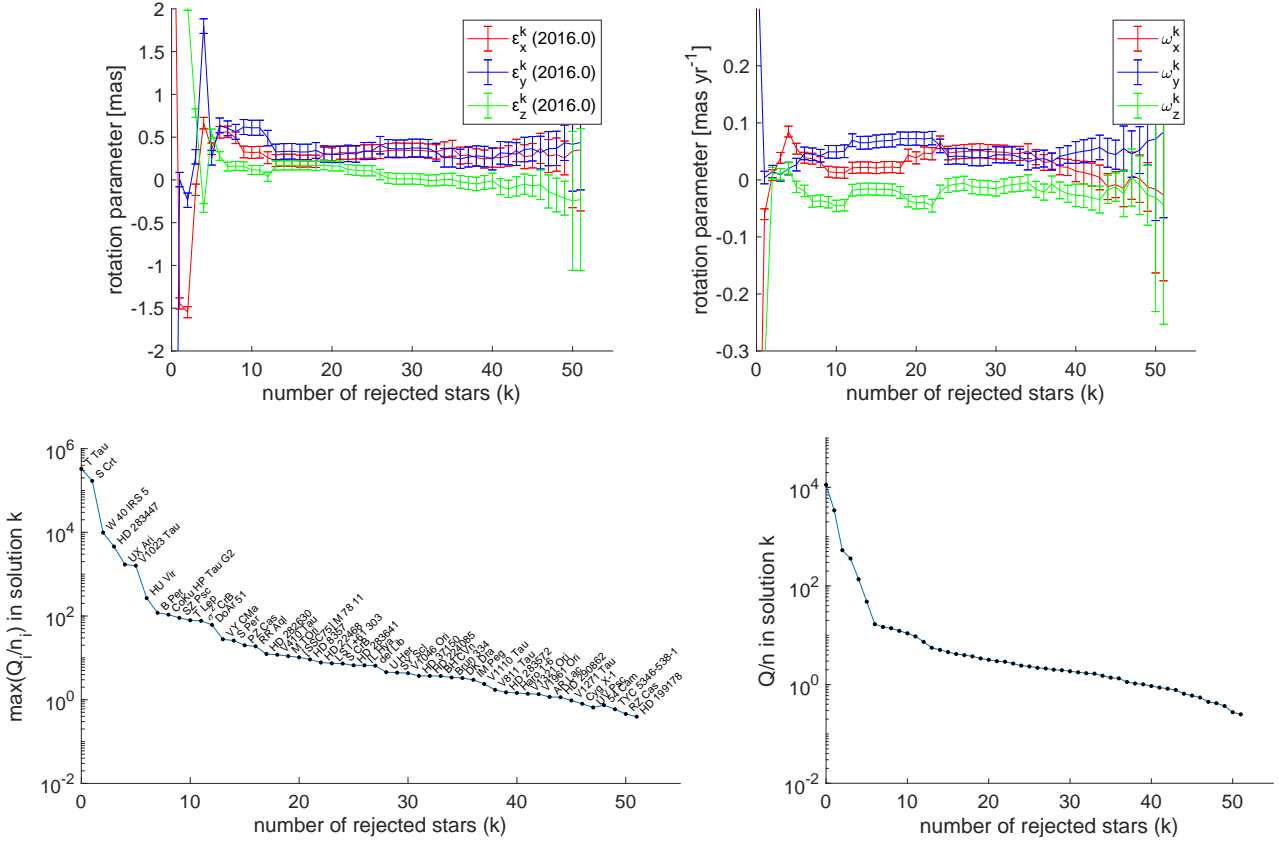


Fig. 3. Results for *Gaia* EDR3 in scenario 55,EDR3 when using the homogenized data set described in Sect. 2.1 as well as the new data acquired for this work as explained in Sect. 2.2, with the more realistic errors from Sect. 3.2 applied. For a description of the plots, refer to Fig. 1.

solution from one scenario) can be selected. For this purpose, it is best to choose an iteration solution with as many stars as possible involved, but when a somewhat steady solution is reached – that means, after which the fluctuation of the rotation parameters lies within their level of uncertainties. On the other hand, Q/n should not deviate largely with respect to the next iteration solution anymore, and because Q_i/n_i may reflect the influence of binarity and radio-optical position offsets of the stars, it should be made sure that the stars with excessively large values of Q_i/n_i are not included.

In the case of 41,DR2, if a baseline solution had to be chosen, the one with $k=9$ rejected stars would be selected. This is because the above mentioned metrics, the rotation parameter offsets, the Q/n , and the Q_i/n_i , do not show large jumps anymore when rejecting even more stars. The rotation parameters from this baseline solution are provided in Table E.4. The Q/n for this solution is 4.75, slightly lower than the value in Lindegren (2020b) of 5.68. However, if rejecting 15 stars as done in Lindegren (2020b), the Q/n from our solution would be as low as 2.26, which reflects the improvement resulting from the homogenization and the increase in uncertainties for the absolute positions in scenario 41,DR2. The correlation coefficients between the rotation parameters from the baseline solution are

$$\text{corr}[\epsilon_X(T), \epsilon_Y(T), \epsilon_Z(T), \omega_X, \omega_Y, \omega_Z] = \begin{bmatrix} +1.000 & +0.419 & +0.276 & +0.173 & +0.119 & +0.031 \\ \dots & +1.000 & +0.372 & +0.052 & +0.315 & +0.046 \\ \dots & \dots & +1.000 & +0.033 & +0.125 & +0.113 \\ \dots & \dots & \dots & +1.000 & -0.007 & +0.345 \\ \dots & \dots & \dots & \dots & +1.000 & -0.065 \\ \dots & \dots & \dots & \dots & \dots & +1.000 \end{bmatrix}, \quad (15)$$

which shows that the orientation parameters are still weakly correlated (correlation coefficients up to 0.4). The largest changes in correlation coefficient compared to the Lindegren (2020b) baseline solution happened for that between the orientation and spin parameters in Y (increase by 0.184), and for that between the Y and Z orientation parameters (increase by 0.166).

For scenario 55,DR2 the baseline solution can be the one when rejecting $k = 11$ stars, as listed in Table E.4. The rotation parameters agree with each other for the baseline solutions from the scenarios 41,DR2 and 55,DR2, but there is an improvement in their uncertainties for the scenario 55,DR2. The correlation coefficients between the rotation parameters from the baseline solution are

$$\text{corr}[\epsilon_X(T), \epsilon_Y(T), \epsilon_Z(T), \omega_X, \omega_Y, \omega_Z] = \begin{bmatrix} +1.000 & +0.246 & +0.248 & -0.044 & -0.038 & -0.040 \\ \dots & +1.000 & +0.178 & -0.014 & -0.118 & +0.013 \\ \dots & \dots & +1.000 & -0.052 & +0.011 & -0.133 \\ \dots & \dots & \dots & +1.000 & -0.004 & +0.290 \\ \dots & \dots & \dots & \dots & +1.000 & -0.046 \\ \dots & \dots & \dots & \dots & \dots & +1.000 \end{bmatrix}. \quad (16)$$

As shown in this matrix, there are only negligible correlations between the rotation parameters (correlation coefficients smaller than 0.3).

In 55,DR2, the weights of the stars used for solving for the spin are similar to those in scenario 41,DR2, Lind2020, ranging from $0.68 \text{ mas}^{-2} \text{ yr}^2$ to $910 \text{ mas}^{-2} \text{ yr}^2$ with a median of $107 \text{ mas}^{-2} \text{ yr}^2$. The group of stars having the largest weights is the same as that in 41,DR2 and 41,DR2, Lind2020 (see

Lindgren 2020b). The weights of the stars used for solving for the orientation, however, reduce substantially to be within the range of 0.01 mas^{-2} to 54 mas^{-2} , with a median of 9 mas^{-2} . This means that the corresponding stars more evenly contribute to the orientation estimates compared to 41,DR2,Lind2020, where the range of weights was 0.2 mas^{-2} to 1156 mas^{-2} . The contribution to the determination of the orientation parameters with the highest weights are from the stars reobserved in the January 2020 sessions.

For 55,DR2, we also tried employing the barycenter instead of the center of luminosity as a reference point for the new observations of the close unresolved binaries in Table 3 to investigate which center is closer to the *Gaia* photocenter. The differences in the residuals for the astrometric parameters are similar to the position differences between the two centers in Table 3. The residuals are not systematically smaller for either center. However, the study may be biased because the historical positions of the three binary stars (from Lindgren 2020a) included in the VLBI data set have not been changed. A more detailed study needs to be carried out to investigate the change from the barycenter to the center of luminosity also for the historical data. The proper motion values and uncertainties did not change between Lindgren (2020b) and our work. Thus, if the spin were determined only from the proper motion information, it would be the same when using the proper motions of either the 55,DR2 or the 41,DR2,Lind2020 data set. The latter is scenario B in Lindgren (2020b) and the determined spin is $(-0.050, -0.139, 0.002) \pm (0.036, 0.055, 0.038) \text{ mas yr}^{-1}$. The spin from the baseline solution of 55,DR2 (including the information coming from the positions) that is reported in Table E.4 can thus be compared directly to the spin from scenario B to see if the positions have an effect on the determination of the spin. The comparison shows that the spin parameters from the two solutions differs by less than 1σ . However, their uncertainties are about halved in the case of 55,DR2, meaning that the addition of the positions allows the determination of the spin to be improved. For the spin in *Y*, our baseline solution $(-0.113 \pm 0.024 \text{ mas yr}^{-1})$ is closer to scenario B than to the baseline solution of 41,DR2,Lind2020 $(-0.051 \pm 0.027 \text{ mas yr}^{-1})$, equivalent to scenario A in Lindgren 2020b). Compared to 41,DR2,Lind2020, the positions in 55,DR2 were given lower weights relative to the proper motion information because of inflated uncertainties. However, the effect of the inflated position uncertainties was compensated by the increased number of star positions so that the formal errors for the spin parameters in 55,DR2 are similar to those of the original baseline solution 41,DR2,Lind2020.

Another possibility to assess the results of the homogenization effort and the new one-epoch positions is to compare with other results from the literature. Brandt (2018) derived proper motions of 115 662 stars by dividing the differences of positions from *Gaia* DR2 and HIPPARCOS by the time difference of their respective epochs, which is 24.25 yr. In addition, he reduced systematics by cross-calibrating these proper motions with the proper motions from the *Gaia* and HIPPARCOS catalogs themselves. This includes the correction of global rotations between the catalogs. The spin parameters he derived are $(\omega_X, \omega_Y, \omega_Z) = (-0.081, -0.113, -0.038) \text{ mas yr}^{-1}$. Lindgren (2020a) estimated the corresponding uncertainties to be 0.03 mas yr^{-1} . Brandt's spin parameters for *Gaia* DR2 must be corrected for the orientation offset between the *Gaia* DR2 bright frame and ICRF3 in order to compare them to the spin parameters of 55,DR2. This requires adding the orientation parameters of 55,DR2 divided by the time difference of 24.25 yr to the

spin parameters of Brandt (2018; Lindgren 2020a). The corrected spin parameters are $(\omega_X, \omega_Y, \omega_Z) = (-0.077, -0.094, -0.037) \pm (0.026, 0.026, 0.025) \text{ mas yr}^{-1}$. Comparing with the values for 55,DR2 in Table E.4, the differences are at the level of 0.7σ , 0.5σ , and 2.1σ , thus showing reasonably good agreement between the two determinations.

5.3. Alignment of *Gaia* EDR3

The iteration that rejects the 13 most deviating stars is selected as a new baseline solution for 55,EDR3 as given in Table E.4. The uncertainties show a similar behavior as those predicted by Lindgren (2020b) – that is that the spin parameter uncertainties should decrease in future *Gaia* data releases, even without adding further VLBI observations. This is due to smaller uncertainties in the *Gaia* EDR3 positions and proper motions. However, the Q/n equals 5.58 for this solution, which is larger than that for the baseline solution of 55,DR2 at iteration $k = 13$ (4.63), thus signaling the presence of systematic errors. The correlation coefficients between the rotation parameters from the baseline solution are

$$\text{corr}[\epsilon_X(T), \epsilon_Y(T), \epsilon_Z(T), \omega_X, \omega_Y, \omega_Z] = \begin{bmatrix} +1.000 & +0.225 & +0.212 & +0.200 & +0.024 & -0.003 \\ \dots & +1.000 & +0.177 & +0.021 & +0.177 & +0.010 \\ \dots & \dots & +1.000 & -0.007 & +0.039 & +0.023 \\ \dots & \dots & \dots & +1.000 & +0.044 & +0.326 \\ \dots & \dots & \dots & \dots & +1.000 & +0.018 \\ \dots & \dots & \dots & \dots & \dots & +1.000 \end{bmatrix}. \quad (17)$$

Only negligible correlations (i.e., correlation coefficients smaller than 0.3) among the rotation parameters are present except between ω_X and ω_Z .

For the bright reference frame, a correction was applied to its spin in one of the middle iterations of the *Gaia* EDR3 processing (Lindgren et al. 2021b). The correction was derived through comparing the proper motions of *Gaia* EDR3 at that iteration step with those obtained by dividing the position differences between *Gaia* DR2 and HIPPARCOS by the epoch difference of the two catalogs. The applied spin correction is $(-0.0166, -0.0950, +0.0283) \text{ mas yr}^{-1}$. No orientation offset could be applied due to the lack of suitable data to compare with. Due to the involvement of HIPPARCOS positions in the calculations and their $\pm 0.6 \text{ mas}$ uncertainties in aligning to ICRS at epoch J1991.25, the spin of the bright reference frame of *Gaia* EDR3 cannot be determined to better than about $0.024 \text{ mas yr}^{-1}$ per axis using this method (Lindgren et al. 2021b). This is about twice as large as the formal errors of the spin parameters derived in this study. Due to the applied correction, the result of 55,EDR3 can be understood as the residual spin of the corrected *Gaia* bright frame. The residual spin is determined to be significant at the 2.4σ level in *Y* $(+0.065 \pm 0.026 \text{ mas yr}^{-1})$ when the scaling factor $\sqrt{Q/n}$ is applied). Reversing the applied correction by adding it back to the baseline solution results in an original, uncorrected spin in *Gaia* EDR3 of $(+0.005, -0.030, +0.012) \pm (0.024, 0.026, 0.024) \text{ mas yr}^{-1}$. Our study thus suggests that the uncorrected bright *Gaia* EDR3 frame is more consistent with the ICRF3 than the corrected frame and thus that the spin correction based on HIPPARCOS had better not been applied in the *Gaia* EDR3 processing.

In terms of precision, the current tie of the bright reference frame of *Gaia* to ICRF3 is not yet at the required level. For

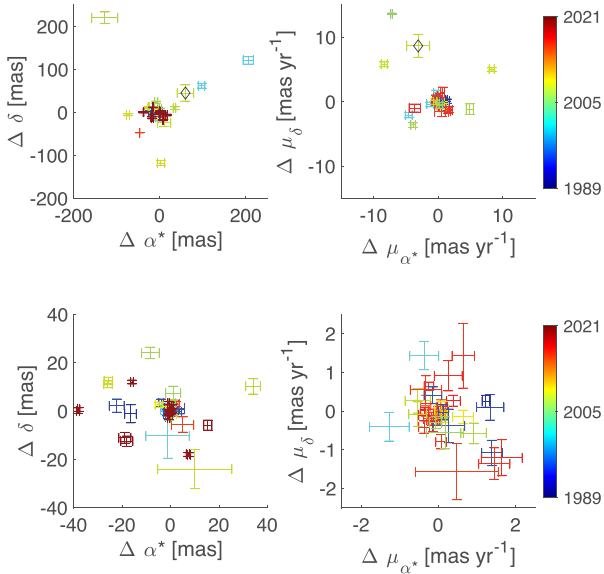


Fig. 4. Residuals of the differences of the positions and proper motions between VLBI and *Gaia* after adjustment of the orientation and spin between the two reference frames. Results are given for the baseline solution of 55,DR2 described in Table E.4. Individual values are color coded by the epoch of the VLBI position. The lower plots show zoomed-in views of the central area of the upper plots. The position residuals for T Tau and S Crb are not shown, as they are outside the plotted area. The residuals for VY CMa are marked with a black diamond.

example, the formal errors of the spin parameters for 55,EDR3 are about 0.01 mas yr^{-1} , which is five times the anticipated $0.002 \text{ mas yr}^{-1}$ proper motion uncertainty for a single star in the final *Gaia* data release⁷, and the $\text{WRMS}_{55,\text{EDR3}}$ values are even larger (see Table 4). Moreover, the parameter estimates do not appear to be very robust (see, e.g., the steadiness of the spin parameters in Fig. 3). Comparing with *Gaia* DR2, the mean errors of the spin parameters are reduced by 50%, an effect due to the increased time span for *Gaia* EDR3, while the mean errors for the orientation parameters remain similar. The WRMS values for *Gaia* EDR3 remain at the same level as that in *Gaia* DR2, or even increase, except for ω_Z . For 55,EDR3, Q/n becomes smaller than unity at $k = 40$, where 15 stars are still included, while for 55,DR2 the value of 1 is reached for $k = 35$, while 20 stars are still included. In all, the increased time span for *Gaia* EDR3 does not translate into an improved frame tie, which indicates that the limitation most probably comes from the VLBI data. Further VLBI observational efforts are therefore highly desirable to improve the current situation.

The residuals of the position and proper motion differences between VLBI and *Gaia* are plotted in Fig. 4 for the baseline solution of 55,DR2 and in Fig. 5 for the baseline solution of 55,EDR3. Apart from a few outliers, most residuals remain within two- to three-fold their uncertainties. The improvement of the *Gaia* proper motion for VY CMa is confirmed. The plots show that the large residuals generally correspond to the stars that have VLBI positions determined from observations at epochs far away from the *Gaia* epoch. This finding suggests that it is best to have VLBI observations concentrated during the *Gaia* observation period.

⁷ <https://www.cosmos.esa.int/web/gaia/science-performance>

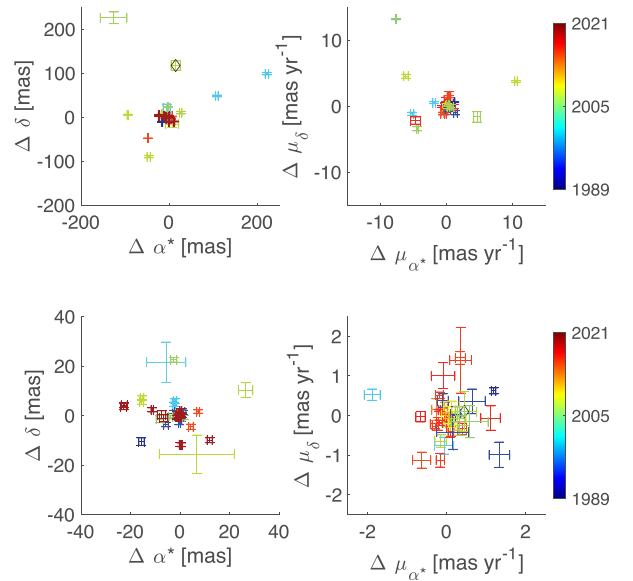


Fig. 5. Residuals of the differences of the positions and proper motions between VLBI and *Gaia* after adjustment of the orientation and spin between the two reference frames. Results are given for the baseline solution of 55,EDR3 described in Table E.4. See Fig. 4 for a description of the plot.

6. Conclusion and outlook

In this work we have evaluated and extended the determination of the orientation and spin of the optically bright ($G \leq 13 \text{ mag}$) *Gaia* reference frame with respect to the ICRF3 as introduced by Lindegren (2020a). We homogenized the data collected in Lindegren (2020a) so that all star positions refer to the ICRF3 and have consistent uncertainties based on the position uncertainty of the calibrators in the ICRF3. Additionally, newly acquired VLBA observations allowed for the detection of 32 stars. The resulting radio positions of these stars were used in our study together with the historical data to further constrain the tie between the two frames. An attempt was also made to evaluate the error budget of the radio positions of the stars with respect to the ICRF3 in order to derive more realistic weights for these positions, which should help further improve the frame tie.

Our study has led to more stable parameter estimates in the iterative process, in which the most divergent star is rejected at each iteration. Moreover, the bright reference frame of *Gaia* DR2, which is estimated to be offset by about 1.3 mas in the Y direction and 0.6 mas in the Z direction by Lindegren (2020b), is now found to agree with the ICRF3 within 0.5 mas in any direction. On the other hand, its spin component in the Y direction is found to be significant at the 2σ level. The newly determined radio positions of 32 stars reduce the correlations among the rotation parameters. Our study further suggests that the bright reference frame of *Gaia* EDR3 is consistent in orientation with the ICRF3 within about 0.3 mas, while its rotation rate is statistically significant, with a magnitude of $0.065 \pm 0.026 \text{ mas yr}^{-1}$ in the Y direction.

Additional VLBI observations, particularly of new stars, will help reduce the formal error of the orientation parameters. The orientation in the Y direction is still the least well determined for both *Gaia* DR2 and *Gaia* EDR3. The observations should be conducted in the immediate future, as observations close to the final *Gaia* epoch will help reduce the formal errors of the orientation parameters most (Lindegren 2020a).

As the optical positions and proper motions of the radio stars will continue to be improved by *Gaia* in the near future, the result of the frame tie will be primarily affected by the astrophysical nature of these stars and the systematic errors in their radio positions with respect to the ICRF3. Although we made an attempt to carefully consider the systematic errors in the process of deriving the results, they are source-dependent and should be assessed on a case-by-case basis. To reduce the impact, it is desirable to acquire further VLBI observations of the known and new stars on a regular basis in the future.

Acknowledgements. We are grateful for the helpful support of F. Schinzel (NRAO) during AIPS data processing. We deeply thank the anonymous referee for constructive suggestions to improve the content and readability of the manuscript. The authors acknowledge use of the Very Long Baseline Array under the US Naval Observatory's time allocation. This work supports USNO's ongoing research into the celestial reference frame and geodesy. We thank also the Socorro correlator for reliably and quickly providing the correlated data. The National Radio Astronomy Observatory is a facility of the National Science Foundation operated under cooperative agreement by Associated Universities, Inc. This project is supported by the DFG grants no. SCHU 1103/7-2 and no. HE 5937/2-2. M.H. Xu was supported by the Academy of Finland project no. 315721. This work has made use of the data from the European Space Agency (ESA) mission *Gaia* processed by the *Gaia* Data Processing and Analysis Consortium as well as from the mission HIPPARCOS. Funding for the DPAC has been provided by national institutions, in particular the institutions participating in the *Gaia* Multilateral Agreement. Calibrators were selected using the NRAO VLBA calibrator search tool (www.vlba.nrao.edu/astro/calib/), the RFC calibrator search tool (www.astrogeo.org/calib/search.html), and the Astrogeo VLBI FITS image database (www.astrogeo.org/vlbi_images/). This research has made use of the VizieR catalog access tool, CDS, Strasbourg, France and the SIMBAD database (Wenger et al. 2000), operated at CDS, Strasbourg, France. Calculations were made in MATLAB which is distributed by the MathWorks, Inc.

References

- Andrei, A. H., Jilinski, E. G., & Puliaev, S. P. 1995, *AJ*, 109, 428
- Arenou, F., Luri, X., Babusiaux, C., et al. 2018, *A&A*, 616, A17
- Arias, E. F., Charlot, P., Feissel, M., & Lestrade, J. F. 1995, *A&A*, 303, 604
- Asaki, Y., Deguchi, S., Imai, H., et al. 2010, *ApJ*, 721, 267
- Barsony, M., Koresko, C., & Matthews, K. 2003, *ApJ*, 591, 1064
- Bartel, N., Bietenholz, M. F., Lebach, D. E., et al. 2015, *Class. Quant. Grav.*, 32, 224021
- Boboltz, D. A., Fey, A. L., Puatua, W. K., et al. 2007, *AJ*, 133, 906
- Boden, A. F., Torres, G., Sargent, A. I., et al. 2007, *ApJ*, 670, 1214
- Brandt, T. D. 2018, *ApJS*, 239, 31
- Carlos, R. C., & Popper, D. M. 1971, *PASP*, 83, 504
- Charlot, P., Jacobs, C. S., Gordon, D., et al. 2020, *A&A*, 644, A159
- Clark, B. G. 1980, *A&A*, 89, 377
- Condon, J. J. 1997, *PASP*, 109, 166
- de Bruijne, J. H. J., Rygl, K. L. J., & Antoja, T. 2014, in *EAS Publications Series*, 67–68, 23
- ESA 1997, The Hipparcos and Tycho catalogues. Astrometric and photometric star catalogues derived from the ESA Hipparcos Space Astrometry Mission, *ESA Special Publication*, 1200
- Folkner, W. M., Williams, J. G., & Boggs, D. H. 2009, *IPN Progress Report*, 178
- Fomalont, E., & Kogan, L. 2005, *AIPS Memo* 111, NRAO
- Fomalont, E., Johnston, K., Fey, A., et al. 2011, *AJ*, 141, 91
- Gaia Collaboration (Brown, A. G. A., et al.) 2016a, *A&A*, 595, A2
- Gaia Collaboration (Prusti, T., et al.) 2016b, *A&A*, 595, A1
- Gaia Collaboration (Brown, A. G. A., et al.) 2018, *A&A*, 616, A1
- Gaia Collaboration (Brown, A. G. A., et al.) 2021a, *A&A*, 649, A1
- Gaia Collaboration (Klioner, S. A., et al.) 2021b, *A&A*, 649, A9
- Galli, P. A. B., Loinard, L., Ortiz-Léon, G. N., et al. 2018, *ApJ*, 859, 33
- Gattano, C., Lambert, S. B., & Le Bail, K. 2018, *A&A*, 618, A80
- Greisen, E. W. 2003, in *Information Handling in Astronomy – Historical Vistas*, 285, ed. A. Heck (Astrophysics and Space Sci Lib: Springer Netherlands), 109
- Högbom, J. A. 1974, *A&As*, 15, 417
- Hummel, C. A., Monnier, J. D., Roettenbacher, R. M., et al. 2017, *ApJ*, 844, 115
- Jones, D. L., Folkner, W. M., Jacobson, R. A., et al. 2020, *AJ*, 159, 72
- Kettenis, M., van Langevelde, H. J., Reynolds, C., & Cotton, B. 2006, in *Astronomical Data Analysis Software and Systems XV*, eds. C. Gabriel, C. Arviset, D. Ponz, & S. Enrique, *Astronomical Society of the Pacific Conference Series*, 351, 497
- Kounkel, M., Hartmann, L., Loinard, L., et al. 2017, *ApJ*, 834, 142
- Kovalev, Y. Y., Lobanov, A. P., Pushkarev, A. B., & Zensus, J. A. 2008, *A&A*, 483, 759
- Kusuno, K., Asaki, Y., Imai, H., & Oyama, T. 2013, *ApJ*, 774, 107
- Lestrade, J. F., Preston, R. A., Jones, D. L., et al. 1999, *A&A*, 344, 1014
- Lindgren, L. 2020a, *A&A*, 633, A1
- Lindgren, L. 2020b, *A&A*, 637, A5
- Lindgren, L., Lammers, U., Bastian, U., et al. 2016, *A&A*, 595, A4
- Lindgren, L., Hernández, J., Bombrun, A., et al. 2018, *A&A*, 616, A2
- Lindgren, L., Bastian, U., Biermann, M., et al. 2021a, *A&A*, 649, A4
- Lindgren, L., Klioner, S. A., Hernández, J., et al. 2021b, *A&A*, 649, A2
- Loinard, L., Torres, R. M., Mioduszewski, A. J., et al. 2007, *ApJ*, 671, 546
- Lunz, S., Heinkelmann, R., Anderson, J., et al. 2019, *Radio source position offsets among various radio frames and Gaia*
- Lunz, S., Heinkelmann, R., Anderson, J., et al. 2020, in *Astrometry, Earth Rotation, and Reference Systems in the GAIA era*, ed. C. Bizouard, 49
- MacMillan, D. S., Fey, A., Gipson, J. M., et al. 2019, *A&A*, 630, A93
- Martí-Vidal, I., Ros, E., Pérez-Torres, M. A., et al. 2010, *A&A*, 515, A53
- Martí-Vidal, I., Ros, E., Pérez-Torres, M. A., et al. 2011, *A&A*, 533, C1
- Martin-Mur, T. J., Zhai, C., Jacobs, C., et al. 2017, in *2017 IEEE International Conference on Space Optical Systems and Applications (ICSOS)*, 176
- Massi, M., Ros, E., Menten, K. M., et al. 2008, *A&A*, 480, 489
- Miller-Jones, J. C. A., Sivakoff, G. R., Knigge, C., et al. 2013, *Science*, 340, 950
- Mioduszewski, A. J. 2009, *AIPS Memo* 110
- Nakagawa, A., Tsushima, M., Ando, K., et al. 2008, *PASJ*, 60, 1013
- Nakagawa, A., Omodaka, T., Handa, T., et al. 2014, *PASJ*, 66, 101
- Nyu, D., Nakagawa, A., Matsui, M., et al. 2011, *PASJ*, 63, 63
- Ortiz-Léon, G. N., Dzib, S. A., Kounkel, M. A., et al. 2017a, *ApJ*, 834, 143
- Ortiz-Léon, G. N., Loinard, L., Kounkel, M. A., et al. 2017b, *ApJ*, 834, 141
- Peterson, W. M., Mutel, R. L., Lestrade, J.-F., Güdel, M., & Goss, W. M. 2011, *ApJ*, 737, 104
- Petrov, L. 2018, VLBI global solution rfc_2018b, http://astrogeo.org/sol/rfc/rfc_2018b/, accessed 2019-06-12
- Phillips, R. B., Lonsdale, C. J., Feigelson, E. D., & Deeney, B. D. 1996, *AJ*, 111, 918
- Porcas, R. W. 2009, *A&A*, 505, L1
- Pradel, N., Charlot, P., & Lestrade, J.-F. 2006, *A&A*, 452, 1099
- Reid, M., & Honma, M. 2014, *ARA&A*, 52, 339
- Riess, A. G., Casertano, S., Yuan, W., et al. 2018, *ApJ*, 861, 126
- Schaefer, G. H., Prato, L., & Simon, M. 2018, *AJ*, 155, 109
- Schönrich, R., McMillan, P., & Eyer, L. 2019, *MNRAS*, 487, 3568
- Secrest, N. J., Dudik, R. P., Dorland, B. N., et al. 2015, *ApJS*, 221, 12
- Secrest, N. J., Dudik, R. P., Dorland, B. N., et al. 2016, *VizieR Online Data Catalog: J/ApJS/221/12*
- Shepherd, M. C. 1997, in *Astronomical Data Analysis Software and Systems VI*, eds. G. Hunt, & H. Payne, *Astronomical Society of the Pacific Conference Series*, 125, 77
- Thompson, A. R., Moran, J. M., & Swenson, G. W. 1986, *Interferometry and Synthesis in Radio Astronomy* (New York: Wiley)
- Titov, O., & Krásná, H. 2018, *A&A*, 610, A36
- Titov, O., Lambert, S. B., & Gontier, A. M. 2011, *A&A*, 529, A91
- Titov, O., Shu, F., & Chen, W. 2020, in *Astrometry, Earth Rotation, and Reference Systems in the GAIA Era*, ed. C. Bizouard, 173
- Torres, R. M., Loinard, L., Mioduszewski, A. J., & Rodríguez, L. F. 2007, *ApJ*, 671, 1813
- Torres, R. M., Loinard, L., Mioduszewski, A. J., & Rodríguez, L. F. 2009, *ApJ*, 698, 242
- Torres, R. M., Loinard, L., Mioduszewski, A. J., et al. 2012, *ApJ*, 747, 18
- van Leeuwen, F. 2007, *A&A*, 474, 653
- Walker, R. C. 2014, *VLBA Scientific Memorandum*
- Welty, A. D. 1995, *AJ*, 110, 776
- Wenger, M., Ochsenbein, F., Egret, D., et al. 2000, *A&As*, 143, 9
- Wrobel, J. M., Walker, R. C., Benson, J. M., & Beasley, A. J. 2000, *VLBA Scientific Memorandum, NRAO*, 24
- Xu, M. H., Wang, G. L., & Zhao, M. 2012, *A&A*, 544, A135
- Xu, M. H., Anderson, J. M., Heinkelmann, R., et al. 2019a, *ApJS*, 242, 5
- Xu, S., Zhang, B., Reid, M. J., Zheng, X., & Wang, G. 2019b, *ApJ*, 875, 114
- Zhang, B., Reid, M. J., Menten, K. M., & Zheng, X. W. 2012, *ApJ*, 744, 23
- Zinn, J. C., Pinsonneault, M. H., Huber, D., & Stello, D. 2019, *ApJ*, 878, 136

Appendix A: Selection of candidate stars and calibrators for new observations

After collecting suitable VLBI data of stars from relevant literature, we conducted a crossmatch between VLBI and *Gaia* by exploiting capabilities of the *Gaia* archive⁸ in order to identify counterparts. We mainly made use of the literature collections of Lindegren (2020a), as well as Xu et al. (2019b), and references therein. Stars that are probably not suitable for the radio-optical link, such as Mira-type stars and red supergiants (Lindegren 2020a) and stars of spectral types other than A, F, G, and K (Lindegren, June 2019, priv. comm.), were rejected. The sample was restricted to stars brighter than $G = 13$ mag having a full 5-parameter solution in DR2. Furthermore, only objects with declinations above -30° were considered because of the declination limit of the VLBA.

Using the RUWE parameter (calculated from *Gaia* DR2 data; Lindegren et al. 2018), we selected stars that were not indicated to be resolved binaries in DR2. For groups of stars within a few degrees on the sky, we selected only the brightest stars at radio frequencies, as multiple detections clustered in one part of the sky are geometrically worse for the determination of the rotation parameters than spreading the observations over the whole sky considering limited telescope time availability. Nine stars were included in the observation proposal although they do not fully meet all selection criteria. Among these are, σ^2 CrB and UX Ari, which were excluded in the analysis of Lindegren (2020b) because they show evidence for a binary companion. However, they are well observed objects in Lestrade et al. (1999), and therefore by extending their position time series with just a few new observations, highly accurate proper motions in the radio frame can be derived along with any nonlinear orbital motions if necessary. Plots of the sky and magnitude coverage of the selected subset, as well as further information on selection criteria, can be found in Lunz et al. (2020). In total 46 stars were chosen as candidates for re-observation.

Criteria for scheduling phase-referencing observations in nodding-style described in Wrobel et al. (2000) were considered. Phase-referencing calibrators that are compact, radio-bright, and close in direction to the target stars were selected, and the ideal switching times between the calibrators and targets were determined. In case historical data used a different calibrator, we added the original phase-referencing calibrator whenever appropriate. In addition, secondary calibrators were chosen whenever possible. These can be utilized for removing residual phase-gradients during the data processing. The recommendations of geometrical arrangements of the secondary calibrators with respect to the primary calibrator and star in Fomalont & Kogan (2005) were followed. Sometimes there were no other suitable calibrators available, whereupon no secondary calibrator was selected.

Appendix B: Peak intensities

For the derivation of peak intensities, phase- and amplitude-self-calibration was performed in AIPS on the phase-referencing calibrator *P1* (see Table 1). With this step, absolute positional information is lost, but the dynamic range in the images increases. More importantly, the phase coherence for the target star is improved, and the accuracy of the flux density measurement is increased. The derived corrections of phase and amplitude were applied to the respective target stars, the secondary calibrators,

and the phase-referencing calibrator itself, in the multisource file. Then, the target stars and secondary calibrators were split and imaged again as described above. If necessary and possible, phase-only self calibration was performed on the target and secondary calibrators afterward. At the end, the peak flux densities of all objects were determined using the task JMFIT on the brightest component based on the image. For the star del Lib, the radio source J1456–0617 was used as the final phase-referencing calibrator because it had more valid fringes than J1510–0843.

For the detected stars and their calibrators, the peak intensities PI are listed in Table B.1. The mean (median) peak intensity for the detected target stars is 11 (1.5) mJy beam⁻¹. Their mean (median) standard deviation σ_{PI} , which represents the RMS noise of the images, is 0.17 (0.09) mJy beam⁻¹. Dynamic ranges DR vary from 5.5 for star SV Cam to 349.6 for SZ Psc.

⁸ <https://gea.esac.esa.int/archive/>

Table B.1. Peak intensities for the 32 detected stars and their calibrators from the VLBA observations conducted on 6-7 January 2020.

Star	PI	σ_{PI}	DR	P_1	PI	σ_{PI}	P_2	PI	σ_{PI}	S_1	PI	σ_{PI}	S_2	PI	σ_{PI}
UV Psc	0.62	0.08	7	J0121+0422	807.58	0.61	J0110+0714	67.72	0.20	J0105+0600	116.37	0.33
HD 8357	0.85	0.09	9	J0121+0422	807.58	0.61	J0110+0714	67.72	0.20	J0130+0842	230.50	0.55
LS I +61 303	8.47	0.13	64	J0244+6228	260.92	0.14	J0306+6243	147.06	0.46
RZ Cas	1.29	0.09	14	J0243+7120	71.22	0.06	J0319+6949	154.53	0.54
bet Per	2.16	0.10	23	J0313+4120	573.17	0.39	J0310+3814	367.41	0.94
UX Ari	10.00	0.14	72	J0316+2733	176.58	0.14	J0329+2756	194.00	0.84
HD 22468	57.99	1.36	43	J0339-0146	541.15	0.09	J0337+0137	26.67	0.22
HD 283447 Ab	1.74	0.07	23	J0408+3032	138.46	0.14	J0403+2600	597.28	3.51	J0421+2606	43.85	0.13
HD 283447 Aa	1.54	0.07	21
B Per	0.95	0.09	11	J0359+5057	5586.50	7.69	J0413+5250	80.94	0.37
V410 Tau	1.66	0.06	27	J0429+2724	224.89	0.16	J0421+2606	43.85	0.13	J0433+2905	95.94	0.22
HD 283572	1.30	0.09	14	J0429+2724	126.58	0.09	J0421+2606	80.94	0.37	J0433+2905	71.08	0.09
T Tau N	2.31	0.06	41	J0428+1732	159.75	0.16	J0423+2108	137.31	0.44
CoKu HP Tau G2	1.25	0.05	24	J0438+2153	119.40	0.13	J0426+2350	190.85	19.09
Brun 334	6.90	0.13	55	J0529-0519	132.23	0.14	J0541-0541	462.99	0.94
TYC 5346-538-1	0.53	0.06	9	J0542-0913	242.02	0.18	J0541-0541	462.99	0.94
SV Cam	0.45	0.08	5	J0626+8202	639.00	0.70	J0637+8125	37.51	0.20
54 Cam	1.48	0.08	19	J0811+5714	341.35	0.25	J0752+5808	31.63	0.14
IL Hya	1.24	0.11	12	J0923-2135	171.68	0.25	J0921-2618	918.36	6.25
HU Vir	1.33	0.09	15	J1216-1033	178.52	0.14	J1204-0710	95.84	0.69
DK Dra	3.62	0.09	40	J1220+7105	315.64	0.13	J1243+7442	248.67	0.58
RS CVn	1.52	0.08	20	J1308+3546	693.90	0.65	J1317+3425	289.24	0.23
BH CVn	3.96	0.10	38	J1324+3622	62.61	0.07	J1340+3754	52.36	0.02	J1322+3912	89.55	0.23
del Lib	0.75	0.09	8	J1456-0617	75.14	0.06	J1510-0843	288.43	1.47	J1512-0905	1686.30	1.66
σ^2 CrB	9.45	0.20	48	J1613+3412	2917.40	1.27	J1558+3323	111.30	0.17
Haro 1-6	4.23	0.15	29	J1633-2557	176.83	0.07	J1625-2527	692.65	0.69
DoAr 51 Aa	1.08	0.07	16	J1633-2557	176.83	0.07	J1625-2527	692.65	0.69
DoAr 51 Ab	1.06	0.07	15
HD 199178	51.90	0.89	58	J2102+4702	121.17	0.09	J2114+4634	134.96	0.29
SS Cyg	0.83	0.11	8	J2136+4301	165.23	0.10	J2153+4322	213.60	0.12
AR Lac	1.24	0.09	14	J2153+4322	213.60	0.12	J2202+4216	1462.50	5.33	J2207+4316	55.49	3.06
IM Peg	25.32	0.35	73	J2253+1608	12360.00	2.63	J2253+1942	188.37	0.49
SZ Psc	172.00	0.49	350	J2311+0205	41.35	0.46	J2320+0513	706.05	6.26
HD 224085	1.26	0.10	13	J2347+2719	143.57	0.07	J2352+3030	28.44	0.19

Notes. The columns show the peak intensity PI and its standard deviation σ_{PI} , both in units of $mJy beam^{-1}$, for the detected stars along with information about the dynamic range DR of the images and PI and σ_{PI} for their calibrators P_1 , P_2 , S_1 , and S_2 as explained in Table 1. The information was derived from fitting a Gaussian to the object image, on which the corrections derived from self-calibration of the primary calibrator P_1 were applied. For the fitting process AIPS task JMFIT was used. An ellipsis (...) indicates the omission of an entry. Stars HD 283447 and DoAr 51 have two detected components (labeled Aa and Ab).

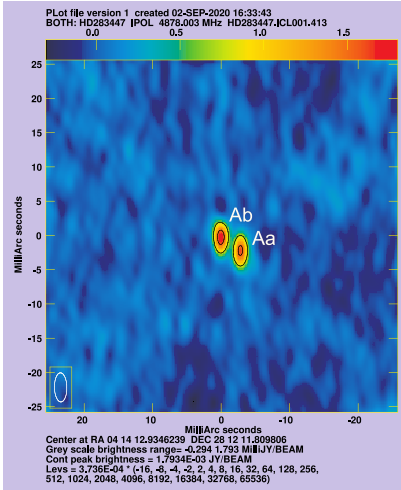


Fig. C.1. Phase-referenced map of star HD 283447. Self-calibration was performed on the calibrator J0408+3032 and applied to the star. The labels Aa and Ab identify the components of subsystem A.

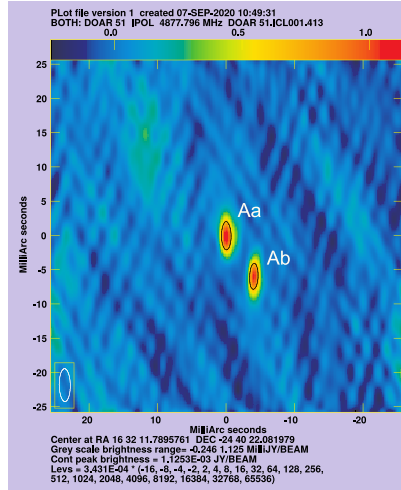


Fig. C.2. Phase-referenced map of star DoAr 51. Self-calibration was performed on the calibrator J1633–2557 and applied to the star. The labels Aa and Ab identify the components of subsystem A.

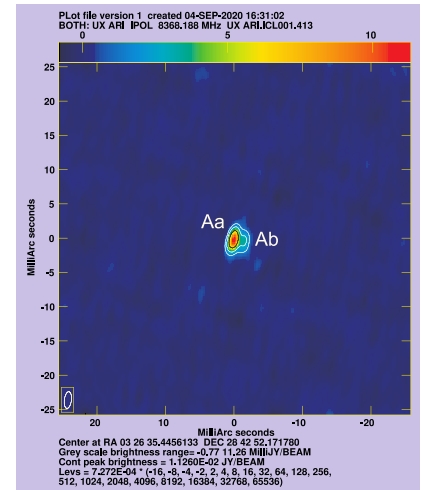


Fig. C.3. Phase-referenced map of star UX Ari. Self-calibration was performed on the calibrator J0316+2733 and applied to the star. The labels Aa and Ab identify the components of the close binary subsystem A.

Appendix C: Identification of close binaries

The VLBI images in Figs. C.1, C.2, and C.3 show that three of our stars are resolved close binaries. Stars HD 283447 (V773 Tau) and DoAr 51 (V2248 Oph) consist of two close components of almost equal peak intensity. As Torres et al. (2012) summarize, HD 283447 is at least a quadruple system. The subsystem HD 283447 A is a strong radio source and a spectroscopic binary consisting of components Aa and Ab (Phillips et al. 1996; Boden et al. 2007; Massi et al. 2008). Its trajectory is gravitationally influenced by the other components of the system, mainly by subsystem HD 283447 B, which has an apparent separation of about 150 mas. From comparison of Fig. C.1 with the orbit (Fig. 4 of Torres et al. 2012), it could be determined that the west (right) component is the primary component Aa, and the east (left) component is the secondary component Ab. DoAr 51 is a triple system with a close binary of about 60 mas maximum separation and a third component about 0.8 away (Barsony et al. 2003; Ortiz-León et al. 2017b). From comparison of the image in Fig. C.2 with the orbit in Fig. 3 of Ortiz-León et al. (2017b), it could be determined that the east (left) component is the primary component Aa, and the west (right) component is the secondary component Ab. For UX Ari, structure was detected, as shown in Fig. C.3, which could represent the inner close binary system A of the triple system described in Hummel et al. (2017). Then the stronger eastern (left) component is the subgiant primary star Aa, and the weaker western (right) component is its main-sequence companion Ab as reported in Carlos & Popper (1971). JMFIT was unable to fit two separate Gaussians, which is why only one component is shown in Table B.1.

Appendix D: Rotation parameter solution using homogenized positions and uncertainties for the calibrators

The recalculation of the rotation parameters as in Fig. 3 in Lindgren (2020b), but using homogenized positions and uncertainties for the 41 stars from Sect. 2.1, yields scenario 41,DR2, $\sigma_{\text{model pos}}$ for the Gaia DR2 analysis (Fig. D.1).

The metrics for the evaluation of the iterative solutions are shown in Table D.1. For comparison, the same metrics for scenario 41,DR2,Lind2020 from the original data published in Lindgren (2020a) are shown in Table 4. The homogenization of the positions and uncertainties reduces the WRMS of all parameters except ϵ_X . In particular, the WRMS decreases by a factor of 2 to 4 for ϵ_Y , ϵ_Z , ω_X , and ω_Y . At the same time, the formal errors of the orientation parameters are increased by a factor of 1.5 to 2 while the formal errors of the spin parameters are only marginally affected. Except for ϵ_X , the WRMSs are equal or smaller than the MEs, whereas they were larger (by up to a factor of 3.5) in scenario 41,DR2,Lind2020. The plots in Fig. D.1 confirm that the solutions of the iterations become steadier for most rotation parameters.

The large orientation offset about the Y axis (1.273 mas) reduces to about one third of its original value (0.393 mas), and the one about the Z axis (0.537 mas) vanishes, while ϵ_X remains small (−0.152 mas). In contrast, the magnitude of the spin parameters along the three axes increase. The differences in orientation and spin except for ω_Z are statistically significant applying the t-test.

The parameter Q/n is below unity with $k = 29$ rejected stars in this scenario compared to $k = 33$ rejected stars in scenario 41,DR2,Lind2020, which shows that the VLBI and Gaia data sets align better for more stars now. The order of the rejected stars is almost the same.

Table D.1. WM, WRMS, and ME of the rotation parameters in scenario 41,DR2, $\sigma_{\text{model pos}}$.

Scenario		$\epsilon_X(\text{T})$	$\epsilon_Y(\text{T})$	$\epsilon_Z(\text{T})$	ω_X	ω_Y	ω_Z
41,DR2, $\sigma_{\text{model pos}}$	WM _{41,DR2,$\sigma_{\text{model pos}}$}	-0.152	0.393	-0.017	-0.077	-0.145	0.046
	WRMS _{41,DR2,$\sigma_{\text{model pos}}$}	0.102	0.055	0.035	0.025	0.010	0.025
	ME _{41,DR2,$\sigma_{\text{model pos}}$}	0.059	0.107	0.051	0.023	0.030	0.027

Notes. Scenario 41,DR2, $\sigma_{\text{model pos}}$ is the homogenized solution from Sect. 2.1. Only iterations 9 to 34 were considered in the calculation. For ME_s the last 10 iterations were rejected because the formal errors of the rotation parameters increase substantially if only a few stars are available for the adjustment. Units are in mas for ϵ_X , ϵ_Y , and ϵ_Z and mas yr^{-1} for ω_X , ω_Y , and ω_Z .

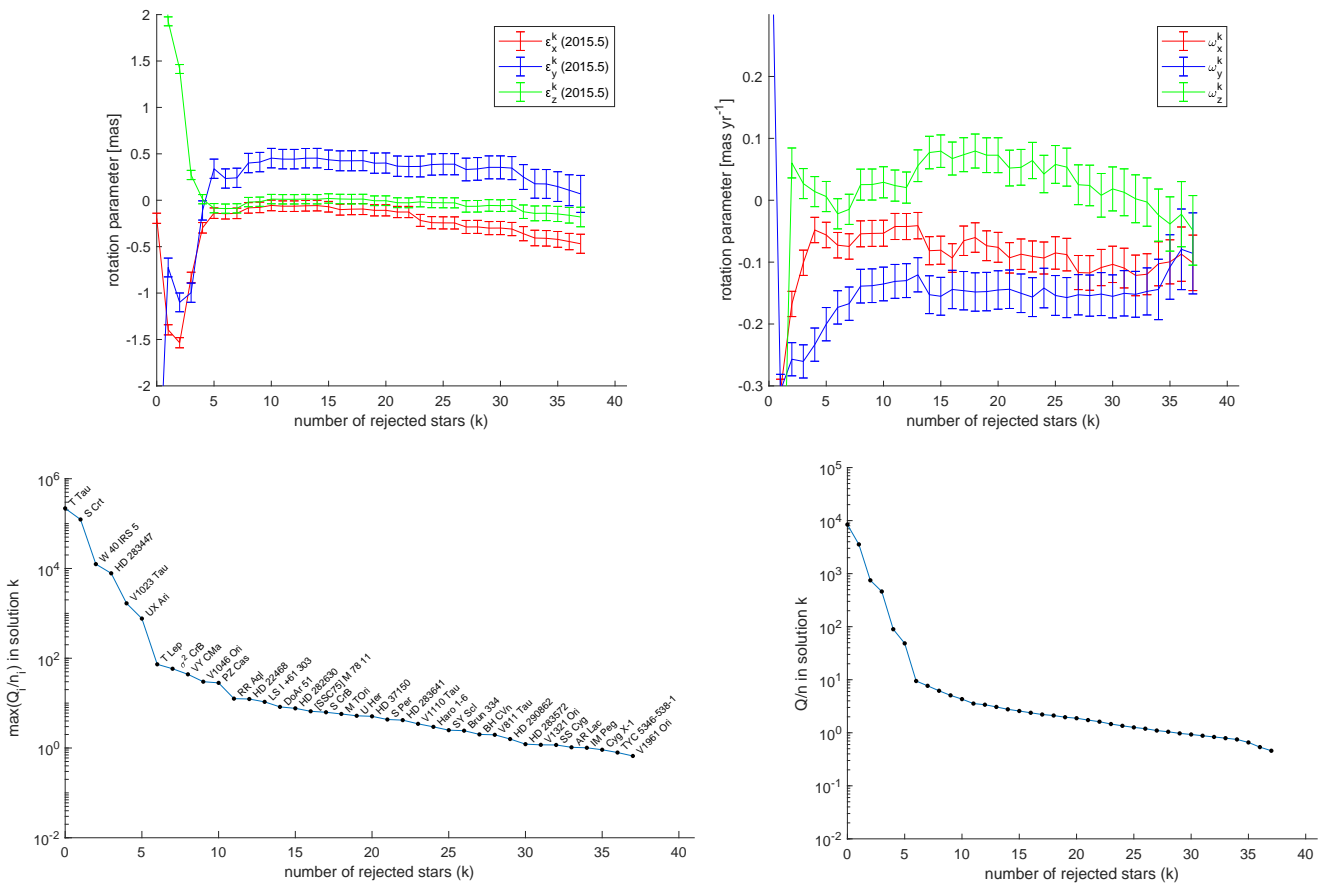


Fig. D.1. Results for the homogenized Lindegren (2020a) data set 41,DR2, $\sigma_{\text{model pos}}$. The upper row shows the orientation and spin parameters for 38 different adjustment solutions, where for each adjustment solution the star with the largest (Q_i/n_i) was rejected in the following iteration. The respective (Q_i/n_i) and the star names are given in the lower-left plot. The lower-right plot represents the quality of the fit, equivalent to the χ^2 of the adjustment, the so-called Q/n .

Appendix E: Tables

Table E.1. Subset of stars from Table 1 of [Lindgren \(2020a\)](#) along with the corresponding phase-referencing calibrators and the corrections to be applied in order to homogenize the data set.

Star Name	Phase-referencing calibrator		Shift to ICRF3 [mas]				Resource	Ref.	
	Name	$\alpha_{original}$ [°]	$\delta_{original}$ [°]	$\Delta\alpha$	$\sigma_{\alpha,CRF}$	$\Delta\delta$			$\sigma_{\delta,CRF}$
SY Scl	J0011 – 2612	2.755194738	–26.209271344	–0.0039	0.0382	0.2940	0.0360	publication	1
S Per	J0222 + 5848 ⁽¹⁾	35.639670150	58.803873460	1.9950	0.8600	0.5850	1.0400	publication	2
UX Ari	J0329 + 2756	52.490289271	27.937638614	0.2220	0.1130	–0.2555	0.1108	publication	3
HD 283447	J0408 + 3032	62.084906562	30.541802731	0.0369	0.2728	–0.1985	0.4248	VLBA o. a.	4
V410 Tau	J0429 + 2724	67.470669867	27.410521200	0.0167	0.0411	0.1813	0.0443	VLBA o. a.	5
V1023 Tau	J0429 + 2724	67.470669825	27.410521189	–0.1333	0.0411	0.1413	0.0443	VLBA o. a.	6
HD 283572	J0429 + 2724	67.470669825	27.410521189	–0.1333	0.0411	0.1413	0.0443	VLBA o. a.	6,5
T Tau	J0428 + 1732	67.148473662	17.539885553	–0.0353	0.1173	0.4301	0.2328	publication	7
HD 283641	J0429 + 2724	67.470669867	27.410521200	0.0167	0.0411	0.1813	0.0443	VLBA o. a.	5
V1110 Tau	J0435 + 2532	68.894095596	25.549915803	–0.1518	0.1214	–1.6523	0.2062	VLBA o. a.	5
HD 282630	J0459 + 3106	74.887640446	31.109524306	–0.6429	0.1211	–0.7672	0.1622	VLBA o. a.	5
T Lep	J0513 – 2159	78.454643017	–21.987803342	0.0123	0.0748	0.0920	0.1159	publication	8
V1961 Ori	J0529 – 0519	82.473056042	–5.328226883	–0.7522	0.1145	0.1458	0.2271	publication	9
Brun 334	J0529 – 0519	82.473056042	–5.328226883	–0.7522	0.1145	0.1458	0.2271	publication	9
V1321 Ori	J0529 – 0519	82.473056042	–5.328226883	–0.7522	0.1145	0.1458	0.2271	publication	9
MT Ori	J0539 – 0514	84.999738300	–5.244806039	0.8051	0.3541	–1.1310	0.7662	publication	9
V1046 Ori	J0539 – 0514	84.999738300	–5.244806039	0.8051	0.3541	–1.1310	0.7662	publication	9
HD 37150	J0539 – 0514	84.999738300	–5.244806039	0.8051	0.3541	–1.1310	0.7662	publication	9
TY C5346-538-1	J0542 – 0913	85.732822533	–9.225279611	–0.9450	0.1595	–1.0675	0.2860	publication	9
HD 290862	J0558 – 0055	89.684964417	–0.918589931	–1.8798	0.2988	5.3974	0.4889	publication	9
[SSC75] M 78 11	J0558 – 0055	89.684964417	–0.918589931	–1.8798	0.2988	5.3974	0.4889	publication	9
VY CMa	J0725 – 2640	111.351721250	–26.675744444	–0.9074	0.1500	–0.5828	0.3357	publication ⁽²⁾	10
S Cr	J1147 – 0724	176.964808479	–7.411428081	0.0022	0.0331	0.0866	0.0364	publication	11
Haro 1-6	J1627 – 2426 ⁽³⁾	246.750025782	–24.444573598	–0.3121	0.1971	–2.0066	0.4999	VLBA o. a.	12
DoAr 51	J1627 – 2426 ⁽³⁾	246.750025782	–24.444573598	–0.3121	0.1971	–2.0066	0.4999	VLBA o. a.	12
W 40 IRS 5	J1826 + 0149	276.604421567	1.827810811	0.5072	0.0912	–0.5268	0.1718	VLBA o. a.	13
SS Cyg	J2136 + 4301	324.100026608	43.028464750	0.4542	0.1515	–0.5418	0.1450	VLBA o. a.	14
IM Peg	J2253 + 1608	343.490616401	16.148211374	–0.0594	0.0340	0.0665	0.0357	publication ⁽⁴⁾	15
PZ Cas	J2339 + 6010	354.838021708	60.169958056	0.2008	0.1773	–0.5795	0.0864	publication	16

Notes. Listed are only the 29 stars that need homogenization. Right ascension $\alpha_{original}$ and declination $\delta_{original}$ are coordinates from the original publications. The shifts in right ascension $\Delta\alpha$ and declination $\Delta\delta$ must be subtracted from the original coordinates $\alpha_{original}$ and $\delta_{original}$ to match the ICRF3 coordinates. The quantities $\sigma_{\alpha,CRF}$ and $\sigma_{\delta,CRF}$ are the uncertainties of the calibrator coordinates in ICRF3, to be applied as uncertainties for the star coordinates. The last two columns list the resource where the coordinates most likely used in the original publication were found, which can be the VLBA observation archive (VLBA o. a.) or the original publication, and the reference of the original publication. ⁽¹⁾Not in ICRF3. The position used is from rfc_2018b. ⁽²⁾Correct position, obtained from correspondence with main author. ⁽³⁾The position used is from the ICRF3 K-band catalog. ⁽⁴⁾Publication directs to ICRF2, which was therefore used to get the original position.

References. (1) [Nyu et al. \(2011\)](#); (2) [Asaki et al. \(2010\)](#); (3) [Peterson et al. \(2011\)](#); (4) [Torres et al. \(2012\)](#); (5) [Galli et al. \(2018\)](#); (6) [Torres et al. \(2007\)](#); (7) [Loinard et al. \(2007\)](#); (8) [Nakagawa et al. \(2014\)](#); (9) [Kounkel et al. \(2017\)](#); (10) [Zhang et al. \(2012\)](#); (11) [Nakagawa et al. \(2008\)](#); (12) [Ortiz-León et al. \(2017b\)](#); (13) [Ortiz-León et al. \(2017a\)](#); (14) [Miller-Jones et al. \(2013\)](#); (15) [Bartel et al. \(2015\)](#); (16) [Kusuno et al. \(2013\)](#).

Table E.2. Date and time of experiments.

Exp	Date	Start (UTC)	End (UTC)
UL005B (B)	06 January 2020	09:40:41	13:35:10
UL005C (C)	06 January 2020	16:54:30	21:48:40
UL005A (A)	07 January 2020	01:08:09	06:06:27

Table E.3. Positions estimated for the 32 radio stars detected with the VLBA on 6–7 January 2020, along with the respective phase-referencing calibrators used.

Star	Calibrator	Δ_c	Epoch t	$\alpha(t)$	$\sigma_{\text{res,random}}$	$\sigma_{\text{res,absolute}}$	$\delta(t)$	$\sigma_{\delta,\text{random}}$	$\sigma_{\delta,\text{absolute}}$	$Roe(t)$	$\Delta\alpha(t)$	$\Delta\delta(t)$	v_r
		[$^\circ$]	[Julian year]	[$^\circ$]	[mas]	[mas]	[$^\circ$]	[mas]	[mas]	[s]	[mas]	[mas]	[km s^{-1}]
UV Psc	J0121+0422	2.7	J2020.01506	19.230136917	0.051	0.286	6.818181818	0.113	0.700	38	+12.911	+5.221	+6.5
HD 8357	J0121+0422	3.1	J2020.01507	20.737009593	0.032	0.283	7.420541599	0.072	0.694	52	+20.111	+8.046	+12.7
LS I +61 303	J0244+6228	1.3	J2020.01520	40.131930495	0.007	0.315	61.229330180	0.030	0.701	251	+0.755	-0.055	-41.4
RZ Cas	J0243+7120	1.8	J2020.01520	42.231326331	0.011	0.315	69.634498545	0.041	0.714	244	+36.696	-3.523	-39.4
bet Per	J0313+4120	1.0	J2020.01541	47.042232516	0.014	0.283	40.955640671	0.042	0.692	294	+0.053	-0.001	+4.0
UX Ari Aa	J0316+2733	2.5	J2020.01542	51.647690075	0.016	0.429	28.714492103	0.040	0.825	316	+17.162	+1.687	+50.7
...	J0329+2756	1.1	J2020.01542	51.647689970	0.017	0.297	28.714491777	0.043	0.700	316	+17.162	+1.687	+50.7
UX Ari Ab	J0316+2733	2.5	J2020.01542	51.647689596	0.041	0.431	28.714492021	0.103	0.830	316	+17.162	+1.687	+50.7
...	J0329+2756	1.1	J2020.01542	51.647689491	0.038	0.299	28.714491711	0.096	0.705	316	+17.162	+1.687	+50.7
HD 22468	J0339+0146	2.5	J2020.01545	54.196857481	0.017	0.282	0.586857856	0.041	0.692	275	+24.820	+12.618	-15.3
HD 283447 Aa	J0408+3032	2.7	J2020.01544	63.553893394	0.070	0.376	28.203279915	0.174	0.829	380	+5.662	+0.172	+16.0
...	J0403+2600	3.3	J2020.01544	63.553893460	0.071	0.291	28.203280346	0.175	0.713	380	+5.662	+0.172	+16.0
HD 283447 Ab	J0408+3032	2.7	J2020.01544	63.553894285	0.069	0.375	28.203280449	0.171	0.828	380	+5.662	+0.172	+16.0
...	J0403+2600	3.3	J2020.01544	63.553894350	0.070	0.291	28.203280911	0.175	0.713	380	+5.662	+0.172	+16.0
B Per	J0359+5057	3.1	J2020.01544	64.561289604	0.025	0.284	50.295190728	0.077	0.695	359	+9.379	-2.636	+19.8
V410 Tau	J0429+2724	2.7	J2020.01546	64.629671674	0.053	0.287	28.454348214	0.127	0.703	385	+5.467	+0.100	+19.9
HD 283572	J0429+2724	2.0	J2020.01547	65.495256404	0.030	0.284	28.301662284	0.073	0.695	385	+5.374	+0.082	+14.2
T Tau	J0428+1732	2.5	J2020.01548	65.497657029	0.054	0.306	19.534875498	0.126	0.739	384	+4.538	+0.902	+19.2
CoKu HP Tau G2	J0438+2153	1.2	J2020.01549	68.975719888	0.056	0.303	22.903662821	0.133	0.724	403	+3.762	+0.425	+16.6
...	J0426+2350	2.3	J2020.01549	68.975720024	0.056	0.304	22.903662788	0.135	0.722	403	+3.762	+0.425	+16.6
Brun 334	J0529+0919	1.2	J2020.01560	83.665661456	0.055	0.307	-5.407113861	0.135	0.739	398	+0.947	+1.161	+20.3
TYC 5346-538-1	J0542-0913	1.1	J2020.01561	85.640320727	0.102	0.337	-8.120884591	0.252	0.788	393	+0.843	+1.210	+0.0
SV Cam	J0626+8202	0.6	J2020.01461	100.331305792	0.010	0.283	82.266505083	0.074	0.695	249	+9.525	-10.055	-13.8
54 Cam	J0811+5714	1.1	J2020.01358	120.648721430	0.026	0.300	57.273297738	0.050	0.700	399	-4.114	-5.469	+27.5
IL Hya	J0923-2135	2.2	J2020.01348	141.203985240	0.023	0.302	-23.826489207	0.067	0.740	268	-5.425	+2.240	-7.3
HU Vir	J1216-1033	1.7	J2020.01371	183.336147857	0.029	0.306	-9.079682807	0.072	0.740	75	-6.256	+2.836	-0.7
DK Dra	J1220+7105	1.5	J2020.01362	183.922718144	0.006	0.308	72.551058090	0.045	0.702	211	-19.756	-0.529	-45.3
RS CVn	J1308+3546	0.5	J2020.01370	197.653442180	0.023	0.283	35.934999284	0.067	0.694	106	-8.380	+2.342	-13.6
BH CVn	J1324+3622	2.1	J2020.01370	203.699807328	0.016	0.319	37.182358583	0.050	0.726	71	-24.780	+8.029	+6.4
...	J1340+3754	1.3	J2020.01370	203.699807107	0.020	0.318	37.182358180	0.059	0.737	71	-24.780	+8.029	+6.4
del Lib	J1456-0617	2.1	J2020.01405	225.242763734	0.036	0.312	-8.518981969	0.081	0.702	-243	-6.828	+2.608	-38.7
...	J1510-0843	2.5	J2020.01405	225.242763508	0.035	0.350	-8.518981571	0.078	0.827	-243	-6.828	+2.608	-38.7
σ^2 CrB	J1613+3412	0.4	J2020.01416	243.668436106	0.015	0.282	33.858120828	0.031	0.691	-171	-33.406	+30.348	-14.7
Haro 1-6	J1633-2557	2.3	J2020.01429	246.512495673	0.050	0.319	-24.393536461	0.147	0.789	-395	-4.894	+0.436	-3.7
DoAr 51 Aa	J1633-2557	1.3	J2020.01429	248.049123210	0.071	0.322	-24.672800585	0.209	0.803	-402	-4.624	+0.348	+0.0
DoAr 51 Ab	J1633-2557	1.3	J2020.01429	248.049121991	0.077	0.324	-24.672802148	0.228	0.808	-402	-4.624	+0.348	+0.0
HD 199178	J2102+4702	3.0	J2020.01452	313.473754647	0.014	0.394	44.386404314	0.037	0.753	-160	+5.098	+7.566	-30.8
SS Cyg	J2136+4301	1.3	J2020.01451	325.670208442	0.052	0.305	43.586257891	0.113	0.714	-128	+6.921	+6.743	-62.0
AR Lac	J2153+4322	3.5	J2020.01460	332.169653346	0.020	0.297	45.742508506	0.046	0.701	-90	+21.812	+17.103	-33.8
...	J2202+4216	3.6	J2020.01460	332.169653266	0.021	0.282	45.742508577	0.047	0.692	-90	+21.812	+17.103	-33.8
IM Peg	J2253+1608	0.7	J2020.01469	343.259318421	0.018	0.282	16.841040559	0.041	0.692	-189	+8.023	+5.163	-14.4
SZ Psc	J2311+0205	0.8	J2020.01475	348.349199758	0.029	0.471	2.675591665	0.065	1.106	-211	+8.955	+4.455	+12.0
...	J2320+0513	3.1	J2020.01475	348.349199839	0.022	0.283	2.675591802	0.047	0.692	-211	+8.955	+4.455	+12.0
HD 224085	J2347+2719	2.1	J2020.01471	358.770517712	0.038	0.303	28.633868049	0.062	0.723	-36	+25.207	+12.003	-20.5

Notes. The apparent star-calibrator separation is Δ_c . Uncertainties $\sigma_{\text{res,random}}$ and $\sigma_{\delta,\text{random}}$ refer to the random error from observations, whereas $\sigma_{\text{res,absolute}}$ and $\sigma_{\delta,\text{absolute}}$ are inflated uncertainties as described in Sect. 3.2. The parameters $Roe(t)$, $\Delta\alpha(t)$, and $\Delta\delta(t)$ need to be applied if the effect of parallax should be corrected. Thereby, the Römer delay Roe needs to be subtracted from the epoch t in column 4, which is the mean epoch between the first and the last scans. In addition, the parallax effects $\Delta\alpha$, and $\Delta\delta$ need to be added to the positions in Cols. 5 and 8. The last column shows the radial velocity (v_r) taken from SIMBAD and used in the rotation parameter calculation.

Table E.4. Baseline solutions for various scenarios.

scenario	k	l	$\epsilon_X(\text{T})$	$\epsilon_Y(\text{T})$	$\epsilon_Z(\text{T})$	ω_X	ω_Y	ω_Z	Q/n
			$\sigma_{\epsilon_X}(\text{T})$	$\sigma_{\epsilon_Y}(\text{T})$	$\sigma_{\epsilon_Z}(\text{T})$	σ_{ω_X}	σ_{ω_Y}	σ_{ω_Z}	
Lindegren (2020b)	15	26	-0.019	+1.304	+0.553	-0.068	-0.051	-0.014	
			0.032	0.074	0.026	0.023	0.027	0.028	5.68
41,DR2	9	32	+0.100	+0.405	-0.044	-0.045	-0.141	+0.023	
			0.099	0.177	0.082	0.022	0.029	0.026	4.75
55,DR2	11	44	+0.093	+0.463	+0.028	-0.056	-0.113	+0.033	
			0.074	0.100	0.058	0.019	0.024	0.022	5.89
55,EDR3	13	42	+0.226	+0.327	+0.168	+0.022	+0.065	-0.016	
			0.070	0.091	0.054	0.010	0.011	0.010	5.58

Notes. The numbers k and l provide the number of rejected stars and the number of stars remaining in the sample for each baseline solution. The σ values indicate the formal errors of the parameter estimates from the baseline solution for each scenario. Final uncertainties are obtained by multiplying the σ values by $\sqrt{Q/n}$. Units are in milliarcseconds for $\epsilon_X(\text{T})$, $\epsilon_Y(\text{T})$, and $\epsilon_Z(\text{T})$ and milliarcseconds per year for ω_X , ω_Y , and ω_Z .